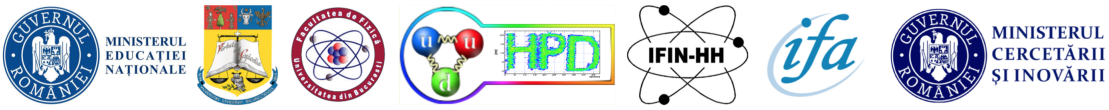

UNIVERSITY OF BUCHAREST

FACULTY OF PHYSICS

MASTER THESIS

Color Glass Condensate Inspired Scaling and Gluon Saturation

Amelia LINDNER

Supervisors:
Prof. Dr. Mihai PETROVICI
Prof. Dr. Alexandru JIPA

Hadronic Physics Department (HPD)
Horia Hulubei National Institute for R&D in Physics and Nuclear Engineering
(IFIN-HH)

June 2019

Abstract

The latest experimental results from RHIC and LHC are used in this thesis in order to study the dependence of different observables on the square root of the hadron multiplicity over unit of rapidity and unit of transverse overlapping area, the Color Glass Condensate inspired scaling variable. The most relevant dependencies on this geometrical variable, like the $< p_T >$, the slopes of $< p_T >$ - mass dependence and the Boltzmann-Gibbs Blast Wave fit parameters will be discussed.

This study was conducted for a large range of energies, from 7.7 GeV, up to 5.44 TeV, for several colliding systems, i.e. Cu-Cu, Au-Au, Pb-Pb and Xe-Xe, based on published experimental data and Glauber Monte Carlo estimates. Signs of gluon saturation are present for the most central collisions for the highest center-of-mass energies available at LHC.

Similarities between small colliding systems (pp) and heavy ion collisions (Pb-Pb) at LHC energies are also reported in this thesis.

Acknowledgements

I would like to express my deepest gratitude to my Supervisor, Prof. Dr. Mihai Petrovici, for his professional guidance, immense knowledge, but most important, for inspiring me with his work ethic and infinite enthusiasm. Furthermore, I would like to thank him for providing me the possibility to work in an incredible research environment, that can only encourage and inspire a young scientist like me.

Further thanks to Dr. Amalia Pop, Dr. Cristian Andrei and Dr. Andrei Herghelegiu for their guidance, suggestions, for their patience and fruitful discussions.

I would also like to express my thanks for all the people in the Hadron Physics Department.

Contents

1 Introduction

High energy heavy ion collisions are the only way to recreate in the laboratory the states of matter supposed to be existing a few microseconds after the Big Bang, in terms of densities and temperatures. In understanding the phenomena produced colliding two heavy ions, one has to consider that the matter will present some finite size effects, it has a violent evolution in time and highly non-homogenous in its initial state. All these have to be considered and be taken into account when the properties of this kind of matter are studied.

The Introduction chapter contains the theoretical framework of this thesis, starting with a short description of the Quantum Chromodynamics (QCD) theory, its properties, the description of the phase diagram of strongly interacting matter and ending with the limitations of the perturbative QCD (pQCD) and a short description of a theoretical model that works in the non-perturbative regime of QCD, the Color Glass Condensate (CGC).

Arguments for studying heavy ion collisions are summarized in the second chapter. Some basic notions about the collision geometry and of the model that describes the heavy ion collisions from the geometrical point of view, i.e. Glauber model, the main research facilities in the heavy ion collisions field and some of the results obtained at RHIC (Relativistic Heavy Ion Collider) and LHC (Large Hadron Collider) are presented. The fourth chapter contains a description of the proton-proton (pp) collisions, considered a very good benchmark for the heavy ion collisions and why are they relevant at the energies reached at LHC. The similarities with heavy ion collisions, are also discussed in this chapter.

In the fifth chapter chapter is introduced the scaling variable inspired by the CGC model and how it was obtained for several colliding systems and center of mass energies that were used in this study. In the sixth chapter are presented the results of the present study and their significance. A summary and the outlook of this thesis are presented in the seventh chapter.

1.1 Quantum Chromodynamics

The evolution of experimental particle physics has lead to the discovery of *quarks*, as the fundamental particles that form all the existing hadrons. The hadrons are composed of three quarks, in the case of baryons, or two quarks, in the case of mesons. The quarks are interacting to each other through the strong force. The particularity that quarks possess in order to be able to participate in the strong interaction is that they are carrying color charges.

The quarks interact to each other through bosons that are mediating the strong interaction, which are called *gluons*, also carrying color charges. This particularity of gluons leads to the fact that they are able to interact with each other, resulting some interesting features that the strong interaction possesses, that will be discussed below.

The field theory of strong interactions is known as Quantum Chromodynamics (QCD), which describes the fields of quarks and gluons and their interactions.

The QCD Lagrangian density is [1]:

$$\mathcal{L}_{QCD} = \sum_f \bar{q}_i^f(x)(i\gamma^\mu D_\mu - m_f)_{ij} q_j^f(x) - \frac{1}{4} F_{\mu\nu}^a F_a^{\mu\nu} \tag{1.1}$$

where q_i^f and $\bar{q_i}^f$ are used for the notations of quark and antiquark (spin -1/2 Dirac), fields of color i,j (red, green, blue), flavour f (up, down, strange, charm, bottom, top) and their associated masses.

The covariant derivative, D_μ is defined by:

$$D_\mu = \partial_\mu - igA_\mu \tag{1.2}$$

$$F_{\mu\nu}^a = \partial_\mu A_\nu^a - \partial_\nu A_\mu^a + g f^{abc} A_\mu^b A_\nu^c \tag{1.3}$$

where A_μ^a are the gluon fields (the spin 1 boson with zero mass and color a), $F_{\mu\nu}^a$ is the non-Abelian gluon field strength tensor, f^{abc} are the structure constants of the color group SU(3) and μ^2 is the energy scale of the process which has an arbitrary value, so it could be equal with the squared four-momentum transfer, Q^2.

1.1.1 Asymptotic Freedom

Experimentally was evidenced that as the quarks within a hadron are getting closer to each other, the strong coupling between them asymptotically approaches zero at short distances, which implies a large momentum transfer. This leads to the phenomenon called *asymptotic freedom* at high momentum transfer and, in the case of a low momentum transfer, to a strong coupling regime. This effect tells us that the quarks inside a hadron behave more or less as free particles, depending on the the amount of momentum transfer (Fig. 1.1).

The running coupling constant is [1]:

$$\alpha_s(Q^2) = \frac{\alpha_s(\mu^2)}{1 + \alpha_s(\mu^2)\beta_2 ln(\frac{Q^2}{\mu^2})} \tag{1.4}$$

where

$$\beta_2 = \frac{11N_c - 2N_f}{12\pi} \tag{1.5}$$

and N_c is the number of colors, while N_f stands for the number of quark flavours.

The behavior of quarks and gluons at large momenta is clear from Eq.1.4, where one can see that $\alpha_s \to 0$ as $Q^2 \to \infty$, which shows that the quarks and gluons are interacting weakly at short distances.

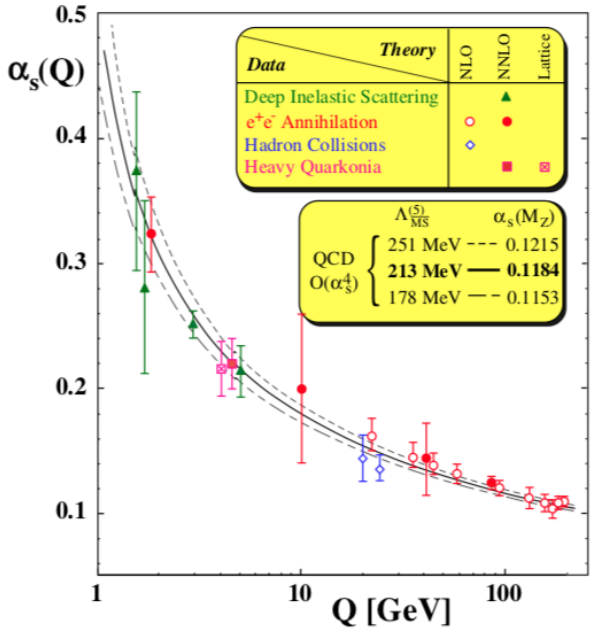

FIGURE 1.1: The running coupling constant, α_s, as a function of the energy scale, Q, and the comparison between experimental data and the theoretical predictions [2].

Due to the asymptotic freedom phenomenon, one can use the perturbation theory for the case of a large momentum transfer, where the perturbative QCD (pQCD) explains rather good the experimental data.

The region where the values of the coupling constant is small enough in order to treat the strong interaction in the perturbative regime is set by the *fundamental scale of QCD*, Λ_{QCD}. The coupling constant of QCD has the following dependence of Λ_{QCD} [1]:

$$\alpha_s(Q^2) = \frac{2\pi}{\beta_0 ln(Q^2/\Lambda_{QCD})} \tag{1.6}$$

where

$$\Lambda_{QCD} \sim 200MeV \tag{1.7}$$

The notions of light and heavy quarks are also defined relative to Λ_{QCD}. One considers the light quarks those flavours with masses much smaller than Λ_{QCD} (up, down), while the heavy quarks are those with masses larger than Λ_{QCD} (charm, bottom, top), the strange quark being an exception, in some cases being treated as light and in others as a heavy quark.

1.2 The Phase Diagram of Strongly Interacting Matter

The thermodynamic properties of a system are expressed in terms of a phase diagram that illustrates the mutual dependence of the thermodynamic parameters of

the system. In the case of QCD, the phase diagram is expressed in terms of the temperature, T, as a function of the baryonic chemical potential, μ_B. Each point of the QCD phase diagram corresponds to a stable thermodynamic state, which is described by specific thermodynamic functions (Fig. 1.2).

Due to the phenomenon of asymptotic freedom of QCD, the phases of QCD that involve high temperatures and high baryonic chemical potentials are better described in terms of quarks and gluons as degrees of freedom.

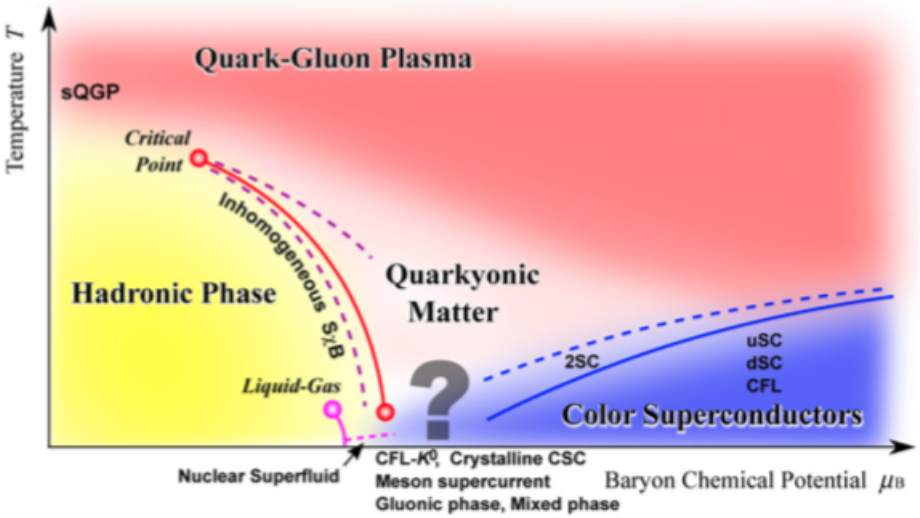

FIGURE 1.2: The phase diagram of QCD [3].

In the first tens of microseconds after the Big Bang, the only part of the phase diagram reached was the zero baryon number density region, as the Universe was cooling down. In this region, QCD lattice simulations can be performed.

The phase transition between the hadronic gas and the matter deconfined in its constituents, quarks and gluons, the so-called partons, has a critical point, characterised by the critical temperature, T_c. In the approximation of two massless quarks, where $m_u = m_d = 0$ and m_s is very large (the chiral limit), the phase transition is one of the second order and for temperatures $T < T_c$, the chiral symmetry is broken by quark masses, while for $T > T_c$, the chiral symmetry is restored. Since in nature the quarks are not massless, the second order phase transition is considered to be a crossover region for $\mu_B = 0$. Also, in the case where m_s has a comparable value to those of the up and down quarks, the phase transition is predicted by the lattice simulations to be a first order transition [4].

Another interesting region of the phase diagram, the region described by high baryonic density matter at low temperatures, dense enough so that it cannot be made of individual well-separated nucleons, even at low temperatures, is supposed to be characteristic for the center of a neutron star. At even lower temperatures and higher densities, i.e. higher baryonic chemical potential, theoretical models predict a new regime of color superconducting quark matter.

1.3 Deep Inelastic Scattering

Since the discovery of quarks and gluons as fundamental particles, the next step was the investigation of the structure of the proton, based on high energy scattering processes.

There are two types of scattering processes in QCD, characterised by the fraction of the momentum exchange in the scattering between probe and the constituent partons of the initial hadron, x. The *soft* interactions are those which correspond to $x \ll 1$ and are non-perturbative processes with large cross sections, while the *hard* interactions are characterised by $x \sim 1$, such as jets, with small cross sections, but because of the asymptotic freedom of QCD, these kind of processes can be treated by pQCD. Since hard interactions are very rare processes, due to the fact that can happen only when in the initial state of the hadron appear in some rare fluctuations, the soft processes provide a very high interest in the field of QCD.

Deep inelastic scatterings (DIS) are *semihard* processes, where only a small amount of energy is exchanged between the probe and hadron's constituents. The semihard processes are providing valuable information because they have cross sections comparable to the size of a hadron, but unlike the soft interactions, this process appears at small transverse distances, so one can observe the physics related to soft interactions in this semihard processes, while the amplitudes of these interactions can be

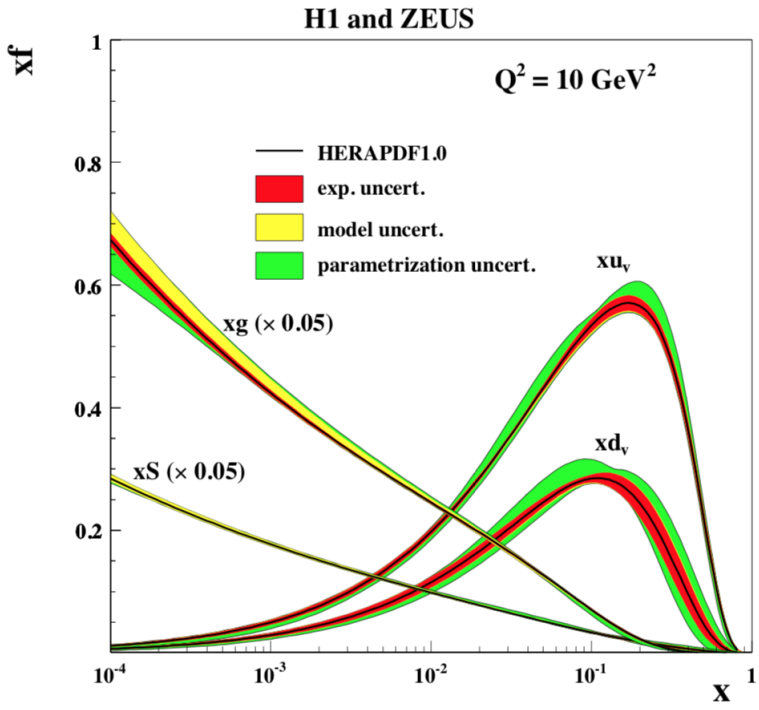

FIGURE 1.3: The contribution of each flavour into the partonic distribution functions of a proton, measured in deep inelastic scattering, at HERA [5].

calculated with pQCD.

The study of deep inelastic scatterings of different charged or neutral leptons on nucleons or nuclear targets have lead to the determination of the parton distributions functions (PDFs), obtained by fitting the experimental data. Since QCD doesn't predict the parton distributions inside a proton. The electron-proton collider at HERA was opening a new landscape, by reaching large range in x and Q^2 [6].

Some of the experimental results obtained at HERA are summarized in Fig. 1.3, in terms of PDFs of a proton at $Q^2 = 10\ GeV^2$, separated into the contribution of each flavour, obtained from the fit parametrisations of the PDFs, which are the gluon distributions (xg), the valence quark distributions (xu_v and xd_v) and the sea quark pairs distributions (xS), which are the main constituents of a hadron, in the infinite momentum frame, described by the *parton model*, in the Bjorken limit.

1.4 Color Glass Condensate

One can observe in Fig. 1.3 that the gluon distribution of a proton rises very fast with decreasing x. The stability of the parton model consists in the maximum occupation number of the gluons to have an $1/\alpha_s$ order where we have a saturation scale, $Q_s(x)$, that increases as x decreases. In this limit, the proton can be considered a dense many body system of gluons (Fig. 1.4). In the Regge-Gribov limit (Q^2 - fixed, x $\rightarrow$ 0), the hadron structures can be observed for $Q^2 \geq 1\ GeV^2$.

Color Glass Condensate (CGC) is an effective field theory where the degrees of freedom are separated into fast frozen color sources and slow dynamical color fields,

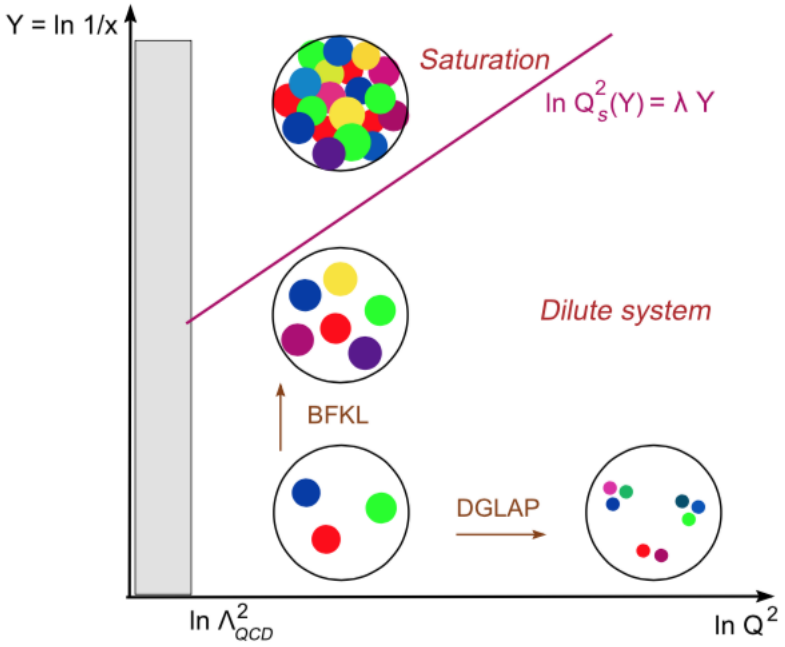

FIGURE 1.4: The phase diagram of the QCD evolution [7].

which describes the properties of matter where gluon saturation is present. The name can be very well understood by analysing it word by word: *color* - the model describes a state of matter made of gluons with colors, *glass* - the gluons are evolving on much longer time scales than the natural time scale, $1/Q_s$, combined with the stochastic nature of sources, and *condensate* - the high density of matter, which has a large occupation number of gluons.

The CGC framework is an important tool because it describes the collective dynamics of QCD at high densities of partons. This model proves the universality of the physics of saturated gluons and shows that it is independent of the fragmentation region, based on the high similarity between protons and heavy nuclei, for the same values of the impact parameter, at high energies. Also, it can describe a wide variety of processes, like e+p, e+A, p+A or A+A collisions.

The motivation of using this CGC model is for understanding the soft QCD dynamics. The CGC is giving an approach in order to study thermalization in heavy ion collisions and also the initial conditions that are standing for the evolution of the thermalized deconfined matter.

2 | Heavy Ion Collisions

Heavy ion collisions represent one of hottest topics of nowadays and the last half of century, with an impressive evolution in both theory and experiments. In the last decades, as soon as ultrarelativistic beams of several types of nuclei or protons became available, the physics beyond these collisions was studied intensively. Without the remarkable progresses in this field of research, the dynamical phenomena or the understanding of the properties of matter described by QCD would have been negligible, due to the strength of the QCD interactions that can't be studied in any other way.

The study of heavy ion collisions gives us the opportunity to have an insight of the mechanisms the particle production in these high energy collisions, where there are still some unanswered questions that date back even before the development of QCD. Initially, the need of heavy ion experiments came with the understanding that the matter that was filling up the universe a few microseconds after the Big Bang had temperatures higher than Λ_{QCD}, so any kind of hadrons were impossible to be produced, the main goal of heavy ion collision experiments being the recreation, in the laboratory, of droplets of this kind of matter. The possibility to recreate this Big Bang characteristic type of matter is giving us the only chance to explore its properties, dynamics, and the phase diagram of QCD.

2.1 High Energy Density versus High Baryon Density

The study of the QCD's phase diagram and the search of its critical point (whose existence was predicted by several theoretical models) are the main goal of heavy ion experiments. The phase diagram is studied in heavy ion collisions at both RHIC and LHC experimental facilities where beams of different types of nuclei are collided, by varying the collision energies, thus the T and μ_B parameters that are describing it (Fig. 1.2).

The highest center of masses energies in these collisions are reached at LHC, where is explored the free baryonic region of the phase diagram, i.e. $\mu_B \approx 0$ and high temperatures, where the predictions of the lattice QCD calculations of reach high energy densities can be verified. The maximum values of the energy density is reached when the two Lorentz contracted nuclei collide. The Lorentz contraction is described by the γ factor, which increases with the center of mass energy. At LHC the reached energy density values are 20 times higher than inside a hadron. Such state of matter, called Glasma [8] is highly coherent and makes the transition from CGC to Quark Gluon Plasma (QGP).The initial longitudinal flux tubes of electric and

magnetic color fields expand outwards, inducing transverse fields strengths decaying into particles. The partons are strongly coupled to each other, forming a state of deconfined matter where they move collectively, a medium that behaves like a relativistic fluid that flows hydrodynamically, whose motion, expansion and cooling depend on its initial high pressure. This state of deconfined matter holds for as long as the energy density in all its volume stays above to that of an individual hadron.

Since this high energy density is not reached in all the volume of the colliding nuclei, there are parts of the initial colliding nuclei that are moving in the forward or backward direction, which form a form of matter that is described by high baryonic density at high values of rapidity. This type of matter expands and hydrodynamizes and it forms a state of deconfined matter which is very rich in quarks, but, unfortunately, it can't be studied due to the experimental limitations of the detectors in this high rapidity regimes.

2.2 The Geometry of a Collision and the Glauber Model

In heavy-ion collisions, the energy and the type of the colliding nuclei are the only parameters that the experimenters have under their direct control, the geometry or the dynamics of the process couldn't be measured directly. Therefore, one has to reconstruct the whole process, event by event, starting from the measured quantities. In the case of colliders, where we work in the center-of-mass frame, due to the Lorentz contraction of the nuclei in the longitudinal direction, we can consider a nucleus as a thin disk with a radius that is approximatively equal to the cube root of the mass number of the corresponding nucleus, $R \simeq A^{1/3}$.

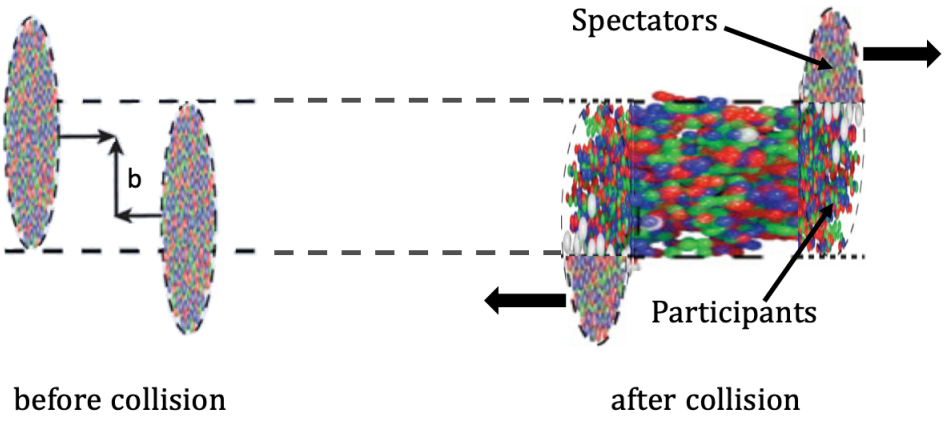

FIGURE 2.1: *Left:* Before collision: two heavy ions with the impact parameter b; *Right:* After collision: the contributions of participants and spectators from the total initial number of nucleons.

One of the most important information of the collision, from the geometric point of view, is the collision *centrality*, which reveals the violence of the collision. This feature is described by the impact parameter, b (Fig. 2.1, left), which is the distance

between the centers of the two colliding nuclei. In the case of a small impact parameter, we have a central collision, and the two nuclei collide almost head-on, while in the case of a large value of the impact parameter, we have a peripheral collision. The extreme limit of the peripheral collisions are the ultraperipheral collisions, where the nuclei pass off each other, but they are still interacting through the electromagnetic fields around them, producing lots of γA and $\gamma\gamma$ interactions that form the bulk nucleus-nucleus (A-A) interaction cross-section.

Another important aspect of the collisions is that there are some nucleons of the initial nuclei that don't encounter any collisions, thus, don't participate in the collision and neither in the particle production process, are called *spectators*, while the remaining nucleons that suffer one or several collisions with other nucleons, are called *participants* (Fig. 2.1, right). Since the participants can suffer more than a single collision, the number of binary collisions (N_{bin}) is larger than the number of participating nucleons (N_{part}), the difference increasing from peripheral to central collisions.

Unfortunately, N_{part} cannot be precisely known, since the number of spectators (N_{spec}) is a quantity that can't be measured directly. The Glauber Model is a theoretical tool that one can use in order to estimate geometrical parameters by simulating the initial conditions of a heavy ion collision for a given value of the impact parameter and for a fixed collision energy.

This model considers the A-A collisions as a collection of many independent nucleon-nucleon (NN) collisions, by making the assumptions that at high energies, the nucleons pass by each other on straight trajectories and could be considered frozen inside the colliding nuclei relative to the very short interaction time. In order to use this model, one needs as an input the nuclear density profile (the Woods-Saxon distribution) (Eq. 2.1) and energy dependence of the non-diffractive, inelastic NN (nucleon-nucleon) cross sections (σ_{inel}^{NN}), which are providing the only dependence on the collision energy for the Glauber calculations [9].

$$\rho(r) = \rho_0 \cdot \frac{1 + w(r/R)^2}{1 + exp(\frac{r-r_0}{a})} \tag{2.1}$$

where r is the distance from the center of the nucleus, r_0 is the mean value of the radius of the nucleus, ρ_0 is the density of nucleons in the center of the nuclei, a is the skin depth and w containes the deviations of the nuclei from a spherical shape; r_0, and a are obtained in low-energy electron scattering experiments, while ρ_0 is obtained from the normalization condition:

$$\int \rho(r) d^3r = A \tag{2.2}$$

There are two different ways to use the Glauber approach: Optical and Monte Carlo. In the optical limit, the nuclei compositions are considered to be uniform over the azimuthal and polar angles, and described by a Fermi distribution in the radial direction. The optical approach is good enough to give us an insight of the geometrical aspects, but it can't provide the location of the nucleons at some specific spatial coordinates so, in order to take into account how the nucleons are spatially distributed inside a nucleus, one has to use the Monte Carlo approach. Also, the optical approach gives a different estimation of the geometrical parameters than the

Monte Carlo one, since is made the approximation that the target is seen by the projectile as a smooth density.

In the Glauber Monte Carlo (GMC) approach, the geometrical parameters are calculated as an average over multiple events, for a specific centrality, by considering a random distribution of the nucleons in the nuclei in each event, according to the nuclear density distribution (Eq. 2.1). Also, the A-A collisions are considered as a sequence of binary NN collisions. The condition that the two nucleons of different nuclei have to satisfy in order to consider that they collide, is [9]:

$$d \leq \sqrt{\frac{\sigma_{inel}^{NN}}{\pi}} \tag{2.3}$$

where d is the transverse distance between the nucleons.

In order to relate the Glauber calculations to the experimental data, since none of the geometrical parameters can be directly determined experimentally, one correlates the number of particle produced in the measured and calculated distribution, by using defining some centrality classes, starting form the assumption that N_{part} is simply related to the impact parameter (Fig. 2.2).

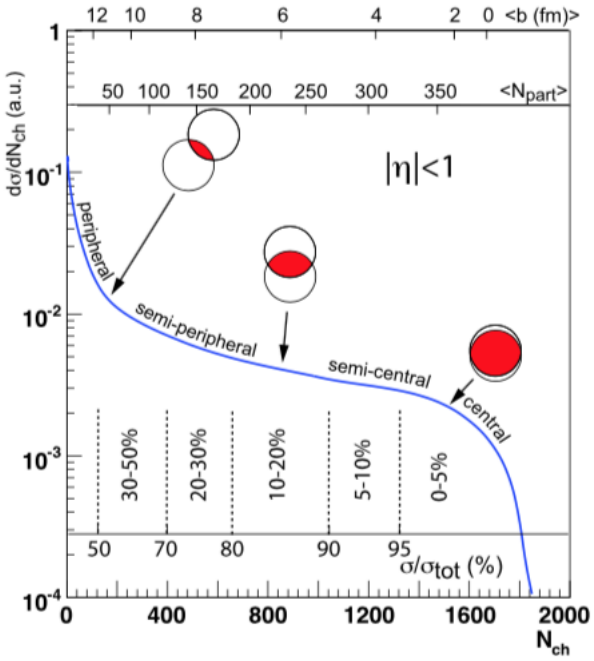

FIGURE 2.2: The correlation between the particle multiplicities and the impact parameter (b) and the number of participants (N_{part}), and the centrality cuts in the multiplicity distribution [9].

From the GMC approach one can calculate the $d\sigma/db$ distribution, and further estimate the total geometric cross section of two colliding nuclei, by integrating these calculated distributions, besides the $< N_{part} >$ and $< N_{bin} >$ quantities, averaged over the different centrality classes. Also, when the cross-section of an interaction

scales with N_{part}, this interaction is considered to be a soft process, while if the cross-section scales with the number of binary collisions, it is considered as a hard interaction.

Another important quantity that can be estimated using the GMC approach is the particle multiplicity, which is a very relevant quantity because it gives information about the energy density reached in the collision. The estimation of this quantity is possible if one assumes that it scales with the number of particle produced in a proton-proton (pp) collision over unit of pseudorapidity (n_{pp}) described by a negative binomial distribution (NBD), by taking into consideration the contribution of both the soft and hard interactions:

$$\frac{dN_{ch}}{d\eta} = n_{pp}[(1-f)\frac{N_{part}}{2} + fN_{bin}] \tag{2.4}$$

where $dN_{ch}/d\eta$ are the number of charged particles produced over unit of pseudorapidity, f is the fraction of the total cross-section that corresponds to hard processes and N_{part} is divided by 2 in order to consider the number of particles produced over the number of participating nucleon pairs.

2.3 The Core-Corona Effect

In the case of ultrarelativistic heavy ion collisions, one of the important things is the correct description of the initial state, since the initial energy density distribution within the fireball is highly non-homogenous, giving rise to fluctuations of different observables. The initial state has to be carefully estimated for the moment when the hydrodynamical expansion starts, since different initial configurations would give different configurations of the final state. Moreover, the initial state configuration has a direct consequence on the description of the dynamics of the collision, up to the kinetic freeze-out moment.

When the collective behaviour is taken into account in heavy ion collisions, one considers the strings that result from the initial scatterings, formed after a proper time, τ_0, which break into segments, identified as hadrons. In the initial configuration that corresponds to τ_0, hot spots of the initial configuration arrise, due to the fact that for a given centrality it was observed that the distribution of the participating nucleons for a given number of collision is highly non-homogenous in the overlapping zone of the colliding nuclei. These hot spots correspond to different density areas, with high-density called *core*, and a low-density, peripheral region, referred to as *corona* [10]. It is very important to have in mind that only the core contribution participates in the collective expansion and the hadronization can be treated statistically, while the corona contribution is represented by the particles produced in nucleon-nucleon collisions [11].

In Refs. [11, 12] a simple model was developed, which separates the number of participants, N_{part}, into two different contributions: core and corona. The corona contribution was considered to consist of the nucleons that suffer only one collision, while the core contribution are the rest of the particles, that form a locally equilibrated source. Based on this model, the centrality dependent multiplicity and $< p_T >$ are quantitatively described by the following equations [11, 12]:

$$M_i^{cen} = N_{part}[f_i^{core} \cdot M^{core})i + (1 - f_{core}) \cdot M_i^{corona}] \tag{2.5}$$

and

$$< p_T >_i^{cen} = [f_i^{core} \cdot < p_T >_i^{core} + (1 - f_i^{core}) \cdot < p_T >_i^{corona}] \tag{2.6}$$

where i stands for different hadron species. The fraction of the core nucleons is denoted with f_i^{core} and, as N_{part}, is estimated using the GMC approach, both quantities being centrality, system size and beam energy dependent. M_{corona} (the multiplicity per corona participant - with $M_{corona} = \frac{1}{2}(dN/dy)^{corona}$) and $< p_{T\,corona} >$ are measured in pp collisions.

The centrality dependence of the fraction of the nucleons that suffer more than a single collision (f_i^{core}) as a function of the total number of nucleons corresponding to the core contribution (f^{core}) is given in the following expression [12]:

$$f_i^{core} = \frac{f^{core} \cdot M_i^{core}}{f^{core} \cdot M_i^{core} + (1 - f^{core}) \cdot M_i^{corona}} \tag{2.7}$$

In Ref. [13] are presented the results obtained for Pb-Pb collisions at $\sqrt{s_{NN}}$ =

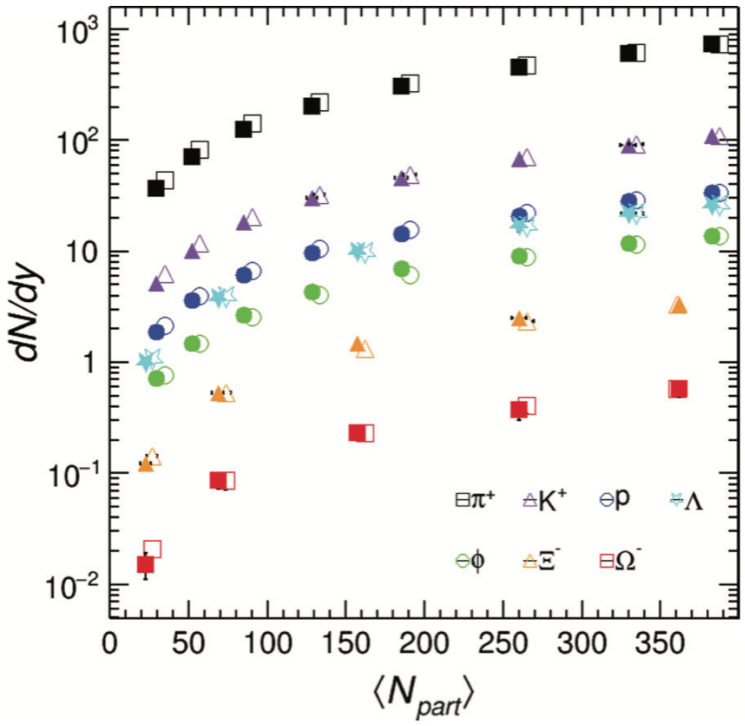

FIGURE 2.3: The estimated hadron yields (for π^+, K^+, p, Λ, ϕ, Ξ^- and Ω^-) as a function of N_{part}, for Pb-Pb collisions at $\sqrt{s_{NN}}$ = 2.76 TeV, for both the experimental values (full symbols) and the core contribution (open symbols); for better visualization, the results related to the core contribution are shifted with 5 units in N_{part} [13].

2.76 TeV when the core contribution is separated from the experimental values and how the core contribution affects different observables that describe the dynamics of the collision, such as $< p_T >$ and the hadron yields. For the corona contribution, the particle yields and $< p_T >$ values correspond to minimum bias proton-proton collisions (pp^{MB}), while the values in terms of multiplicity related to the core contribution (M_{core}) were extracted using Eq. 2.5 for the 0-5% centrality class, for each specie.

In Fig. 2.3, the estimated hadron yields as a function of N_{part} are represented, for both experimental data (full symbols) and core contribution (open symbols). The yields corresponding to the core contribution were estimated based on Eq. 2.5. One can observe that this simple geometrical approach can reproduce rather well the enhancement of light flavour hadron production with increasing centrality.

In terms of the $< p_T >$ values, using Eq. 2.6 and Eq. 2.7 (which translates to Eq. 2.8), Ref. [13] presents a comparison between extracted core values (open symbols) and the experimental data (full symbols) in terms of $< p_T >$ for π^+, K^+, p (Fig. 2.4 - left) and for Λ, Ξ^- and ϕ (Fig. 2.4 - right). The remaining differences could arise from the dependence of p_T distribution on the shape of the fireball, as a function of centrality ($< dN_{ch}/d\eta >$).

$$< p_T >_i^{cen} = \frac{f^{core} < p_T >_i^{core} M_i^{core} + (1 - f^{core}) < p_T >_i^{corona} M_i^{corona}}{f^{core} M_i^{core} + (1 - f^{core}) M_i^{corona}} \tag{2.8}$$

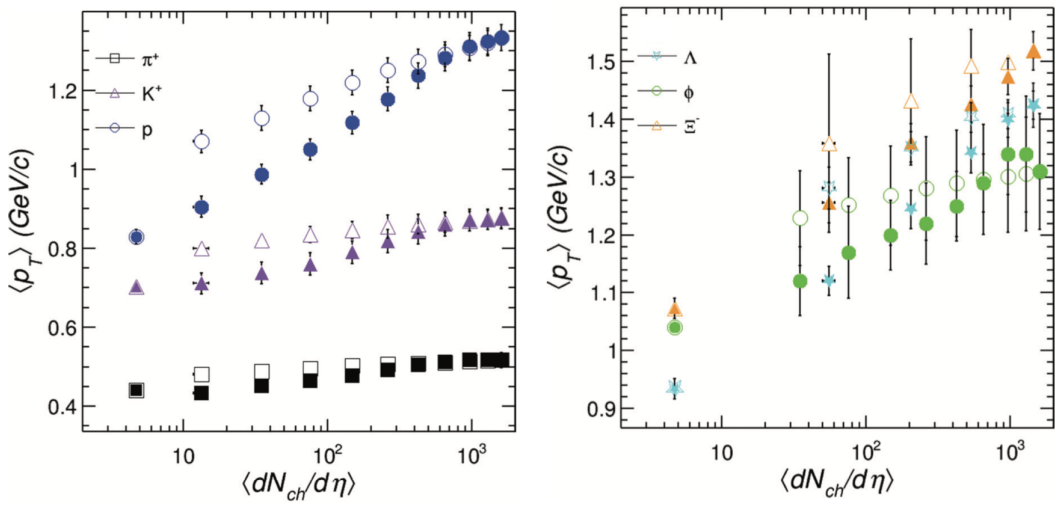

FIGURE 2.4: The $< p_T >$ values as a function of mean charged multiplicity values ($< dN_{ch}/d\eta >$) for experimental data (full symbols) and the corresponding values for the core contribution: *Left:* for π^+, K^+, p; *Right:* for Λ, Ξ^- and ϕ [13].

2.4 Review of the Main Results Obtained at RHIC and LHC

2.4.1 Au-Au Collisions at RHIC: $\sqrt{s_{NN}}$ = 62.4, 130 and 200 GeV

The data taken at the RHIC, starting with 2000, have given for the first time an insight of the state of deconfined matter, described by partonic degrees of freedom and high values of densities and temperatures, obtained in the most central Au-Au collisions at the highest center-of-mass energy available at RHIC, $\sqrt{s_{NN}}$ = 200 GeV. RHIC consists in four experiments, BRAHMS, PHENIX, PHOBOS and STAR, with the two large detectors (PHENIX and STAR) still in operation.

The main goal of this facility was to evidence the existence of deconfined matter, QGP. The soft processes, described by small transverse momentum (p_T) values ($p_T <$ 2 GeV/c), give the information on the energy density, collectivity and the properties of the freeze out stage of the collision (*bulk probes of the medium*), while high p_T ($p_T >$ 6 GeV/c) particles, resulted through hard processes with a very small cross section, such as jets or heavy flavour particles are giving an insight on the properties of the medium (*hard probes of the medium*). The intermediate values of p_T are also revealing some interesting features of these collisions.

By studying the bulk probes of the medium, for different collision energies, centralities and using low p_T identified hadrons, there were evidenced features indicating the formation of the deconfined matter, that presents hydrodynamical expansion. One of the first signs were the values of the energy density reached in these collisions, which were much higher than the values predicted by lattice QCD, obtained from the rapidity dependence of the particle multiplicities. Then, the elliptic flow (v_2), which in heavy-ion collisions describes the azimuthal momentum space anisotropy distribution and is defined as the second harmonic coefficient of a Fourier expansion of the momentum distribution, presents a mass dependence for these low p_T values that corresponds to the hydrodynamical predictions of the QGP equation of state. Also, from the simultaneous fits of the identified particle p_T distributions using Boltzmann-Gibbs Blast Wave (BGBW) expression inspired by hydrodynamical phenomenological models, it was shown that the kinetic freeze-out temperature decreases with the increase of system size, from pp to peripheral A-A, while the transverse expansion increases, which means that the system is cooling down while it expands [14]. The identified particle ratios were also fitted with thermal models in order to obtain the chemical freeze-out temperature and chemical potential, and it was shown that it has a values close to the theoretically predicted critical temperature.

The hard probes, like jets, heavy flavour particles or identified particles with high p_T values, which are relatively rare processes and can be treated through pQCD, being described by large Q^2 values. The most important phenomenon that gives information about the properties of the medium is *jet quenching*, which represents the energy loss of hard partons through the deconfined matter, due to their interactions with the medium. In order to verify the properties of the medium, one has to evaluate the *nuclear modification factor* R_{AA}, which is defined as the invariant p_T spectra of identified or charged particles in A-A collisions, divided by the invariant p_T spectra in pp collisions, at the same collision energy, each one being scaled with

the corresponding number of binary collisions, N_{bin}. If there are no available experimental data for pp collisions, one should evaluate the R_{CP} factor, where the p_T distributions are divided by the most peripheral ones, also scaled by N_{bin}. If there are no nuclear medium effects, the ratio should be one for high p_T values, but, as observed at RHIC, there is a suppression at high p_T values, while in d+Au collisions at the same collision energy, there was observed an enhancement of the R_{AA} values at high p_T, which means that the differences came from final state effects and not due to some differences in the wave functions of the initial state. Also, it was shown that the suppression observed in the most central A-A collisions is not observed in d+Au which is very similar the two particles correlations observed in p+p collisions.

The region described by intermediate p_T values is also very interesting, since at RHIC it was shown that the elliptic flow for light flavour hadrons and hyperons follows a scaling, depending only on the number of constituent quarks (*NCQ scaling*), which means that the elliptic flow arises in the early stages of the deconfinement, when the differences between light and strange quarks are very small. Also, for these p_T values, there was evidenced an enhancement for baryons relative to mesons, due to the higher values of the nuclear modification factor. These effects are contained in the picture in which at the hadronization stage of the collision, quarks and gluons are recombining into hadrons, which is sustained by the recombination models.

Thus, RHIC facility opened a new landscape in Au+Au collisions at the highest center-of-mass energy available, by recreating in the laboratory a state of matter that has partonic degrees of freedom, of which dynamics can be described by hydrodynamical models.

2.4.2 Au-Au Collisions at RHIC: Beam Energy Scan Program

The Beam Energy Scan (BES) program was initiated in order to explore the QCD phase diagram, by covering a relatively wide range of values for the baryonic chemical potential (μ_B), from 100 to 400 MeV (for $\sqrt{s_{NN}}$ = 200 GeV, $\mu_B \approx 0$). The center-of-mass energies measured up to now are $\sqrt{s_{NN}}$ = 7.7, 11.5, 19.6, 27 and 39 GeV. At these energies, besides seeing how the freeze-out processes differ to those at higher energies, one can also study at which energy phenomena like jet quenching, elliptic flow or NCQ scaling no longer hold and also evidence trends expected in the region of a critical point, if it exists.

One of the most interesting result was the behavior of the R_{CP} factor, when mapped for all the RHIC available energies Fig. 2.5. For high p_T values ($p_T > 3$ GeV/c), one can see that for $\sqrt{s_{NN}} \geq 27$ GeV, the R_{CP} values are below unity, which, as mentioned before, is considered an effect of the parton interaction with the highly dense medium. For $\sqrt{s_{NN}} < 27$ GeV, the values of the R_{CP} are increasing with the increase of the energy, which can be considered an energy boundary for the formation of the deconfined matter.

In the case of R_{AA} (or R_{CP}), if one takes into account their dependencies on N_{bin} which was previously presented as an output of the GMC approach, and also the limitations of GMC due to the physical assumptions of it, one can conclude that R_{AA} and R_{CP} are quantities very much affected by model assumptions, so any physical conclusions have to be carefully considered. Furthermore, the GMC approach

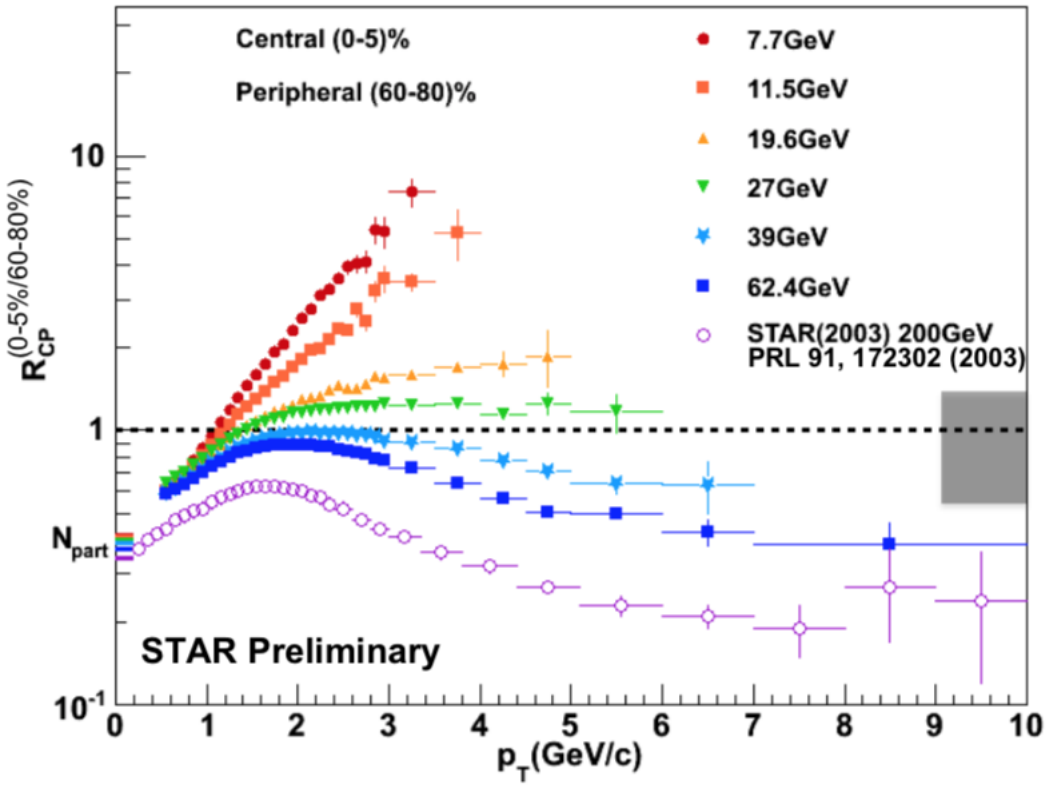

FIGURE 2.5: R_{CP} (0-5%/60-80 %) for charged particle spectra in Au-Au collisions, for energies starting from $\sqrt{s_{NN}}$ = 7.7 GeV, up to $\sqrt{s_{NN}}$ = 200 GeV [15].

is not a viable model for smaller systems, i.e pp, so any comparisons between several collision systems in terms of the nuclear modification factor has to be carefully considered. In order to take into account these effects, in Ref. [16] is presented an observable that can better describe the similarities or differences between different colliding systems, due to the fact that it is free of any model assumptions, being based only on experimental data. In the case of the R_{CP} equivalent, the p_T spectra corresponding to the most central collisions are divided by the p_T spectra corresponding to the most peripheral collisions, but instead of being normalized to N_{bin}, which is a model dependent quantity, the p_T spectra are being normalized to the corresponding average charged particle density, as it follows [16]:

$$\frac{[\frac{d^2N/dp_Tdy}{<dN_{ch}/d\eta>}]^{0-5\%}}{[\frac{d^2N/dp_Tdy}{<dN_{ch}/d\eta>}]^{60-80\%}} \tag{2.9}$$

If one wants to estimate the suppression effect at high p_T values and to see the energy

limit at which this effect no longer appears, unbiased by any model assumption, has to consider the information given in Fig. 2.6, where we have estimated the values of the ratio given in Eq. 2.9, for several colliding systems (Au-Au, Pb-Pb and Xe-Xe) for a wide range of energies (from 7.7 GeV, up to 5.44 TeV) [17–23].

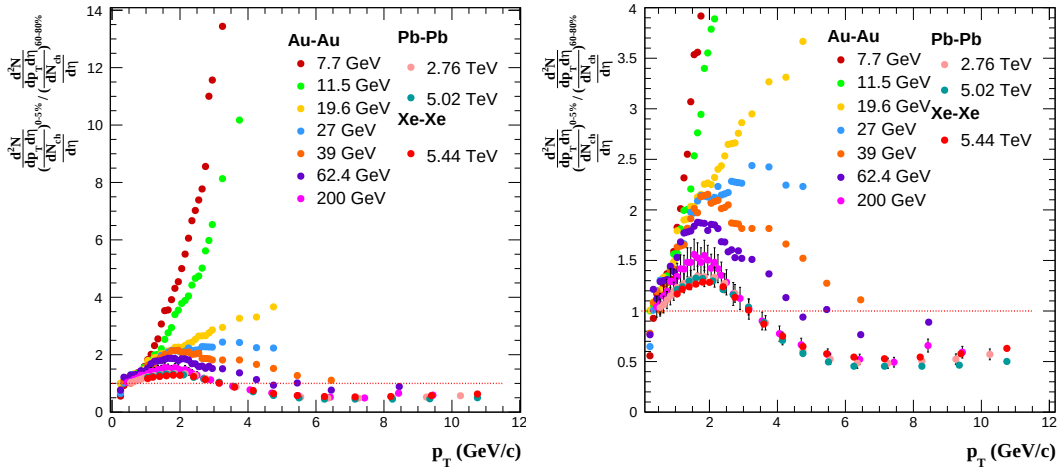

FIGURE 2.6: *Left:* Ratios of p_T spectra of charged particles according to Eq. 2.9 for different collision energies (from 7.7 GeV up to 5.44 TeV [17–23]), for Au-Au, Pb-Pb and Xe-Xe collisions; *Right:* Same as in the left picture, with the values of the ratio given in Eq. 2.9 zoomed in, in order to better observe the suppression effect.

Also, studies of the elliptic flow, v_2, which brings information about the medium in the early stages of the collisions have been performed at these energies, where the NCQ scaling at lower collision energies holds separately, for particles and antiparticles (Fig. 2.7). Such trends seem to indicate that signatures consistent to the deconfined regime disappear or are less significant going towards lower collision energies measured during BES program at RHIC.

The upcoming BES Phase-II will improve the statistics at these low energies, because with the present data the statistics of different observables is not large enough in order to draw definite conclusions. Thus, in BES Phase-II, the statistics at 7.7 and 11.5 GeV are expected to increase, and a proposal of STAR to perform fixed target measurements was released, being the best solution to extend the μ_B range from 400 to 800 MeV.

2.4.3 Pb-Pb & Xe-Xe Collisions at LHC

In this section are summarized some of LHC results obtained in heavy ion collisions. Even if at LHC are in operation four experiments (ALICE, ATLAS, CMS and LHCb), I will focus mainly on the ALICE results, which is the experiment focused on the study of matter at extreme temperatures and densities, where the deconfined matter is formed. For the first Pb-Pb collisions, at $\sqrt{s_{NN}}$ = 2.76 TeV, a comparison was made

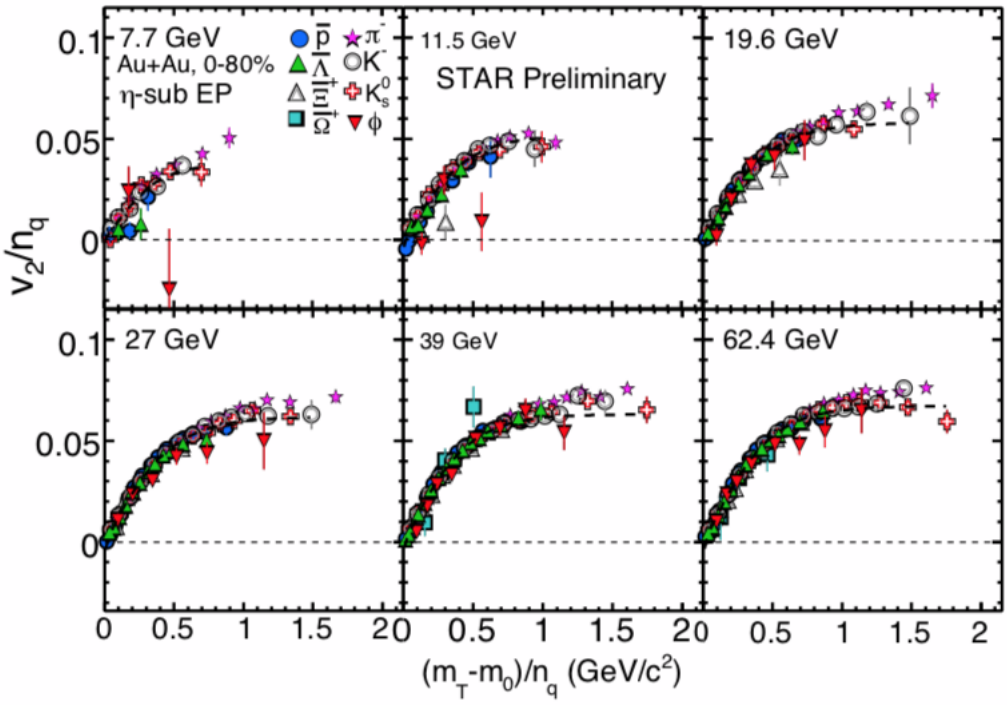

FIGURE 2.7: Elliptic flow NCQ scaling, v_2/n_q, for particles and antiparticles in Au-Au collisions in the 0-80% centrality range, as a function of $(m_T - m_0/n_q)$, where $m_T = \sqrt{m_0^2 + p_T^2}$). [24].

with the results obtained at RHIC, in Au-Au collision, at $\sqrt{s_{NN}}$ = 200 GeV. The energy density produced at LHC is larger than at RHIC, both above the value at which the QCD predicts a phase transition [25]. Also, at this LHC energy, the average multiplicity per number of participants is twice as the RHIC one [26]. For the chemical freeze-out process, the stage of the collision where inelastic processes cease to exist, characterized by particle yields, are described by thermal models within 20% in terms of particle yields ratio, with large deviations for protons and K^{*0}, where processes like re-scattering and regeneration can contribute to the final values, since the the mean lifetime of the particle is smaller than that of the fireball.

Another important feature of the ALICE experiment is its particle identification (PID) capabilities, being specialized in PID from high to low transverse momenta (p_T $\in$ [0.15, 20] GeV/c). Since it's sensitivity to low p_T values and its PID capabilities, the transverse momenta distributions of identified hadrons are used in order to get, besided the particle yields, also important information about the collective expansion of the system at low p_T, to study the presence of new hadronization mechanisms at intermediate p_T and the contribution of the medium on the fragmentation at high p_T values.

In order to understand the shapes of the p_T distributions, one can perform a simultaneous fit of the p_T spectra of different hadrons with a Boltzmann-Gibbs blast

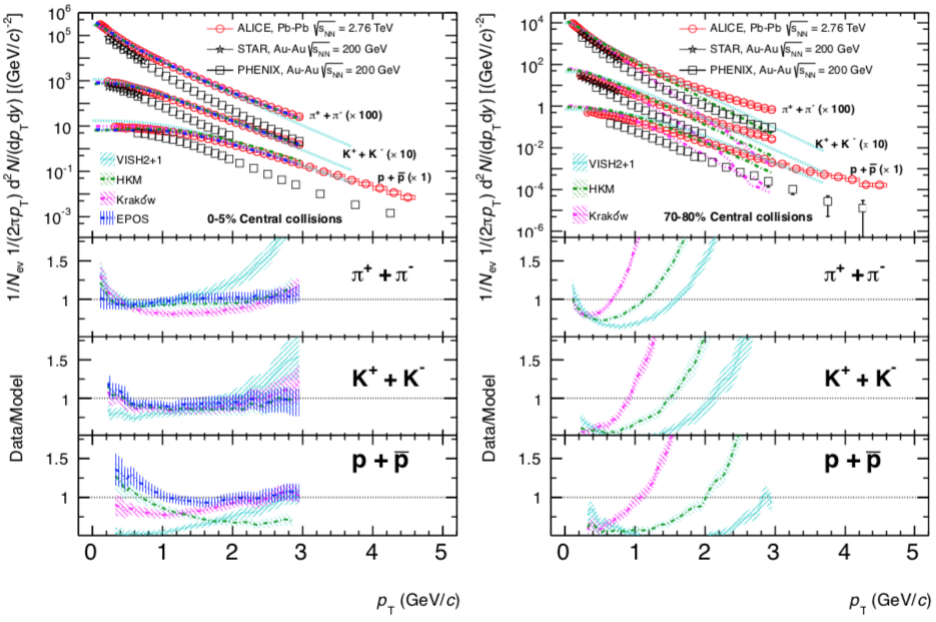

FIGURE 2.8: A comparison in terms of transverse momentum distribution of identified pions, kaons and (anti)protons between RHIC and LHC for central collisions (left) and peripheral collisions (right) [27].

wave (BGBW) expression, inspired from hydrodynamical models [28], from which the kinetic freeze-out parameters are obtained. For Pb-Pb collisions at $\sqrt{s_{NN}}$ = 2.76 TeV, the kinetic freeze-out temperature is similar to that found in Au-Au collisions at $\sqrt{s_{NN}}$ = 200 GeV at RHIC and the radial flow is approximately 10% larger than the one measured at RHIC for most central collisions. Based on this, one can conclude that at LHC is created a hotter system that expands further than at RHIC.

Studies on spatial distributions of decoupling hadrons can no longer be made with a hydrodynamic model, which would affect the estimations in terms of initial temperature of the equation of state of the system. Based on the Hanbury Brown-Twiss (HBT) analysis on intensity interferometry, one can access information related to the expansion rate and spatially distribution at decoupling stage [29]. Based on the HBT radii (which describes the size of the interaction region) that can be extracted from the fit of two pion correlation functions, it was observed that the radii (R_{out} - along the pair transverse momentum, R_{side} - perpendicular to it in the transverse plane and R_{long} - along the beam) of the pion source were larger than those measured at RHIC by 10-35% [29].

In Fig. 2.9 (left) is represented the protons to pions ratio for central collisions Pb-Pb at $\sqrt{s_{NN}}$ = 2.76 TeV. The peak is 20% higher than in the RHIC case, which can be explained by the increase in the average radial flow velocity. This peak is also present in Fig. 2.9 (right), in the kaons to pions particle ratios, which suggests the existence of a strong radial flow. Elliptic flow studies have shown a mass dependence at low p_T values, while for higher p_T values, the elliptic flow seem to have a

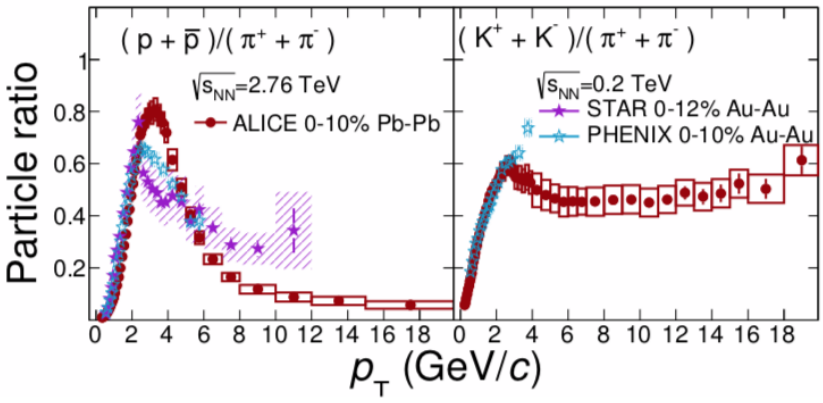

FIGURE 2.9: The comparison between RHIC (Au-Au collisions, $\sqrt{s_{NN}}$ = 200 GeV) and LHC (Pb-Pb collisions, $\sqrt{s_{NN}}$ = 2.76 TeV) in terms of particle yields ratio, protons to pions (left) and kaons to pions (right) [30].

different behavior for baryons and mesons (except for the ϕ meson, that follows the same trend as baryons) [27]. This information gives insight about the behavior of the elliptic flow, that depends on hadron's mass and not on the number of constituent quarks.

The nuclear modification factor R_{AA}, reveals the suppression of particle production in Pb-Pb collisions relative to pp collisions. The elliptic anisotropy of charged jets is also studied in order to obtain information about the path-length dependence of energy-loss, where for the collisional energy loss is linearly proportional to the path-length of particles in the medium, while for radiative energy loss the dependence is quadratic due to interference effects.

Elliptic flow for the D meson, for different centrality classes, shown a decrease from peripheral to central collisions, due to geometrical anisotropy of the initial state. This behaviour supports the idea that the low p_T charm quarks are taking part in the collective motion of the system. The study of R_{AA} and v_2 are made in order to get an insight about the energy-loss in the medium and how is this connected with the transport coefficients.

3 Proton-Proton Collisions at LHC Energies

The interest in colliding systems of different asymmetries and masses came from the need to explore every possible scenario where some kind of effects that could appear in a laboratory environment where these droplets of matter at high temperatures and densities are obtained. In the experiments performed at LHC, the lightest symmetric systems, proton-proton (pp) and the most asymmetric one, proton-nucleus (pA) are used as benchmark systems which are providing information for further understanding of some interesting effects or properties of A-A collisions.

What is interesting nowadays, since pp collisions are performed at LHC energies, is that for the most violent pp collisions, particle multiplicities as those obtained in A-A collisions at RHIC can be reached. More than that, there are strong evidences that some effects that were considered to be characteristic only for A-A collisions, can also be present in pp collisions. These findings increase the interest in studying pp collisions by themselves at LHC energies, not only as references for A-A collisions.

3.1 The Geometry of pp Collisions

As already mentioned, the geometry of a collisions plays an important role in the study of the dynamics of these processes. The values of the impact parameter are very important since they are giving direct information about the amount of energy density produced in A-A collisions. GMC offers a simple geometrical approach of particle production and, based on this, it can give access to impact parameter selection for A-A collisions.

Since the geometry of a system is characterized by the overlapping region of matter, in pp collisions, due to the relatively smaller size of the proton, the spatial distribution of the energy density produced in the collision is very important (Fig. 3.1).

For interactions described by small values of the impact parameter, both hard and soft processes take place and the probability of *Multiple Parton Interactions* (MPI) increases. The study of MPIs is a very important part in the description of inelastic pp collisions. The highest number of MPIs is characteristic to very violent pp collisions, corresponding to small values of the impact parameter (Fig. 3.1).

After the measurement of the topological cross sections for the production of charged particles in pp collisions it was shown that, based on the Koba-Nielsen-Olesen (KNO) scaling law applied on the multiplicity distributions, the shape of the

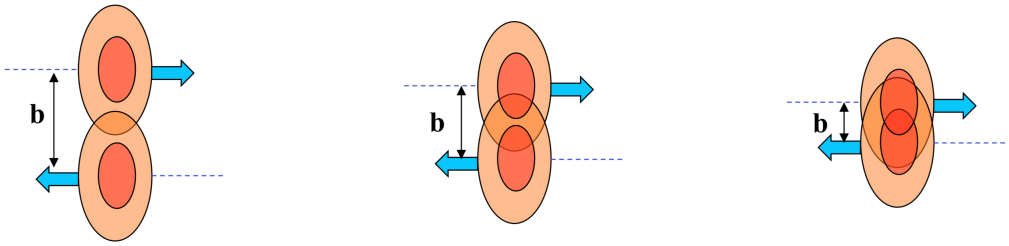

FIGURE 3.1: A sketch of the various types of energy density deposition, from large (left) to small values of the impact parameter (right); red - hard spectrum, orange - soft parton distribution within a proton of ultrarelativistic energies.

scaling function was related to the shape of the topological cross sections. Thus, a study of the correlation between the impact parameter of these high energy elastic hadron scatterings and the KNO function was performed in Ref. [31], where the multiparticle production was treated statistically and the shape of the scaling function was described using a geometrical model approach.

In the description of the geometry of pp collisions, one needs to determine the dependence of the average multiplicity of charged particles produced in a pp collision on the values of the impact parameter, following the phenomenological assumptions presented below [32].

Starting from the general form of the multiplicity distribution:

$$P(n) = \frac{1}{\sigma} \int d^2b\sigma(b)p(n,b) \tag{3.1}$$

with

$$\sigma = \int d^2b\sigma(b) \tag{3.2}$$

where $\sigma(b)$ is the total inelastic cross-section for a given impact parameter (b), σ is the total inelastic cross-section and p(n, b) is the multiplicity distribution of charged particles produced in an event at the same value of the impact parameter [32].

Taking into account the geometrical model that describes the particle production [31] in order to find the properties of the p(n, b) distributions, one can assume that, in the case of high energies, the p(n, b) distribution is narrow [31, 32], which is most likely to be satisfied for the non-diffractive collisions that dominate the inelastic cross-sections:

$$\frac{d(b)}{\overline{n}(b)} \simeq 0 \tag{3.3}$$

with

$$\begin{aligned} \overline{n}(b) &= \sum_n np(n,b) \\ d^2(b) &= \sum_n [n - \overline{n}(b)]^2 p(n,b) \end{aligned} \tag{3.4}$$

where $\overline{n}(b)$ is the average multiplicity and d(b) is the dispersion, both defined for a given value of the impact parameter (b).

With the assumption made in Eq. 3.3, one can find the values of $\overline{n}$ from the experimental data. It is important to mention that the approximation made in Eq. 3.3 was also investigated in Ref. [32] and it doesn't influence the determination of $\overline{n}$.

As shown in Ref. [31], taking into account Eqs. 3.1 and 3.3, one gets:

$$\overline{N}P(n) = \frac{2\pi b\sigma(b)}{\sigma} \frac{\overline{N}}{|\frac{d\overline{n}(b)}{db}|_{b=b_n}} \tag{3.5}$$

which can be considered as a differential equation for $\overline{n}(b)$, so the correlation between the charged particle multiplicity and the impact parameter can be found by solving the following equation:

$$\int_0^{w(b)} \psi(w)dw = \frac{1}{\sigma}\int_b^{\infty} d^2b\sigma(b) \tag{3.6}$$

with

$$\begin{aligned} w(b) &= \frac{\overline{n}(b)}{\overline{N}} \\ \psi(z,\overline{N}) &= \overline{N}P(n) \\ z &= \frac{n}{\overline{N}} \end{aligned} \tag{3.7}$$

where $\overline{N}$ is the average multiplicity of the collision. The $\psi(z,\overline{N})$ function can be obtained from the experimentally multiplicity distributions, for each energy, while $\sigma(b)$, the partial inelastic cross section, is found based on the overlap function (O(b)) [32, 33] and it can be obtained from a double Gaussian matter distribution inside of each of the two colliding protons [34].

Therefore:

$$\sigma(b) = 1 - e^{-kO(b)} \tag{3.8}$$

3.2 Parton Density and Occupation Number in pp Collisions

The study and the description of the early stages of the collisions are one of the most interesting and challenging topics, because are described by large gluon occupation numbers, which suggests that a classical gauge theory description is needed. A general picture is described in Ref. [35], where the gluon number density and occupation numbers, which are considered the general features of the early stage of the collisions, are approximated.

Based on the recipe presented in Ref. [35] for specific experimental data measured at RHIC, one can use these approximations in order to extract the initial gluon number densities and occupation numbers.

If one knows the measured transverse energy dE_T/dy and assuming that almost all the transverse energy is found in gluons, one can make the following approximation [35]:

$$\frac{dE_T}{dy} = [\frac{dN_g^{in}}{dyd^3b} \cdot \Delta b_x]A_g \cdot K \tag{3.9}$$

where with b are denoted the coordinates of a point in the overlapping nuclei, Δb_z is the longitudinal width of the volume occupied by gluons at their time of production, A_g is the area occupied by gluons and K is a gluon transverse momentum. Based on this approximation, the gluon number densities averaged over the production region can be estimated, for an average value of K (for $b_\perp$ = 0 - in the center of the nucleus, $K \simeq Q_s$, where Q_s is the gluon saturation momentum) [35].

More than that, the initial gluon number densities can give an estimation of the gluon occupation numbers, as follows:

$$f_g^{in} = \frac{2\pi^3}{2 \cdot (N_c^2 - 1)} \frac{dN_g^{in}}{d^3 p d^3 b} \simeq \frac{2\pi^3}{2 \cdot (N_c^2 - 1)} \frac{dN_g^{in}}{dy d^2 b_\perp d^2 p_T} \tag{3.10}$$

where the 2 denominator stands for the number of spin states available to gluons and one can consider $\Delta y = \Delta p_z / p_z \simeq \Delta b_z / p_z$; the following approximation also has to be done:

$$\frac{dN_g^{in}}{dy d^2 b_T d^2 p_T} \simeq \frac{1}{\pi Q_s^2} \frac{dN_g^{in}}{dy d^2 b_\perp} \tag{3.11}$$

Following the recipe given in Ref. [35], the following estimates in terms of the gluon number densities of the initial state and of the gluon occupation number have been obtained:

TABLE 3.1: The estimations made on the gluon number densities of the initial state ($\frac{dN_g^{in}}{dy d^2 b}$) and of the gluon occupation number for the most central collisions at the biggest RHIC energy and LHC energies for A-A and highest particle multiplicity for pp collisions at $\sqrt{s}$ = 7 TeV.

System	Au-Au	Pb-Pb		pp
$\sqrt{s}(TeV)$	0.2	2.76	5.02	7
$\frac{dN_g^{in}}{dy d^2 b}$ (fm^{-1})	$\simeq 4.7$	$\simeq 11.8$	$\simeq 15.9$	$\simeq 18.7$
f_{in}^g	$\simeq 0.9$	$\simeq 2.3$	$\simeq 3.1$	$\simeq 3.6$

As one can observe in Table 3.1, a very interesting feature appears at the LHC energies, where the initial gluon number density and occupation number seem to have just a collision energy dependence, while the system size is playing a minor role. This shows that similarities between A-A and pp collisions at LHC energies are expected to be evidenced.

3.3 Review of the Main Results Obtained at LHC in Small Systems and Similarities between pp, p-Pb and Pb-Pb Collisions

The subject of small systems collision at LHC energies received an increased interest lately, since the studies of different observables at high multiplicity in pp collisions

and in asymmetric (p-Pb) collision have revealed some collective-like effects, that were supposed to appear only in A-A collisions.

The CMS Collaboration found a very interesting feature when studying the two-particle correlations in pp at $\sqrt{s}$ = 7 TeV, discovering the long range near side ridge structure in pp collisions at $\sqrt{s}$ = 7 TeV. For low p_T values ($p_T \in$ [1-3] GeV/c) the near side ($\Delta\phi \approx 0$) long range ($2 \leq |\Delta\eta| \leq 4$) correlation was observed [36] (Fig. 3.2 (left)). Also, the p_T spectra of identified hadrons were measured with high precision at ALICE, where at low p_T a hardening is observed in the p_T spectra with increasing multiplicity, feature that is very similar with the radial flow effect observed in heavy ion collisions. More than that, in high multiplicity pp and p-Pb collisions, the p_T spectra are very well described by the BGBW expression, inspired by hydrodynamical phenomenological models.

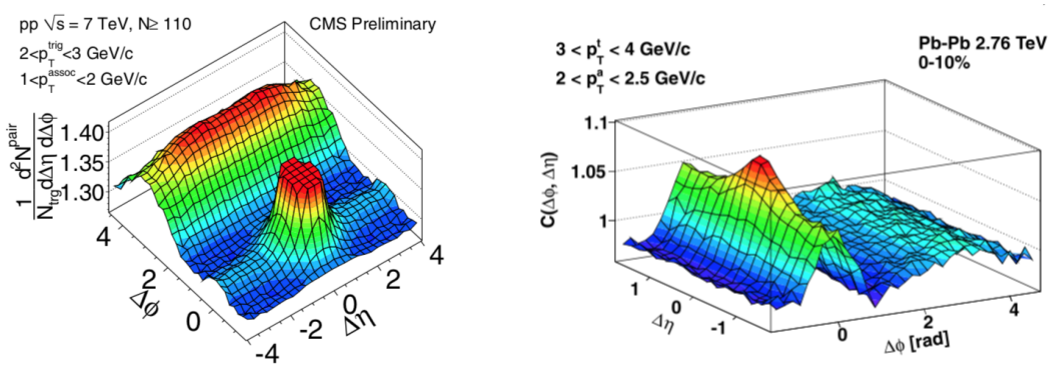

FIGURE 3.2: The comparison of the two particle correlation for high multiplicity pp collisions at $\sqrt{s}$ = 7 TeV(left) [37] and Pb-Pb at $\sqrt{s_{NN}}$ = 2.76 TeV [38], on a finite range of $\Delta\phi$ and $\Delta\eta$.

The enhancement of strange and multi-strange hadron production in pp and p-Pb and its multiplicity dependence was also studied. In Fig. 3.3 can be observed an enhancement of strange to non-strange hadron production relative to pions in high multiplicity pp collisions, which is very similar to that obtained in p-Pb and peripheral Pb-Pb collisions. This enhancement could be a signature of the formation of QGP. However, core-corona relative contribution as a function of centrality could explain most of such a trend [13].

Another interesting effect observed in pp collisions is the depletion at low p_T of proton to pion and proton to kaon ratio, which increases with multiplicity, but decreases towards $p_T \approx$ 1.4-2 GeV/c, feature than in A-A collisions was attributed to a collective transverse flow [39]. More than that, another similarity between pp, p-Pb and Pb-Pb colliding systems was observed in the BGBW fit parameters, the kinetic freeze-out temperature (T_{kin}^{fo}) and the average radial flow velocity ($< \beta_T >$) correlation (Fig. 3.4) [39]. In Fig. 3.4 the T_{kin}^{fo}-$< \beta_T >$ correlation follows the same trend and overlaps in pp at $\sqrt{s}$ = 7 TeV and in p-Pb at $\sqrt{s_{NN}}$ = 5.02 TeV for the same multiplicity classes, while the decrease of T_{kin}^{fo}-$< \beta_T >$ with centrality is much more enhanced in Pb-Pb collisions.

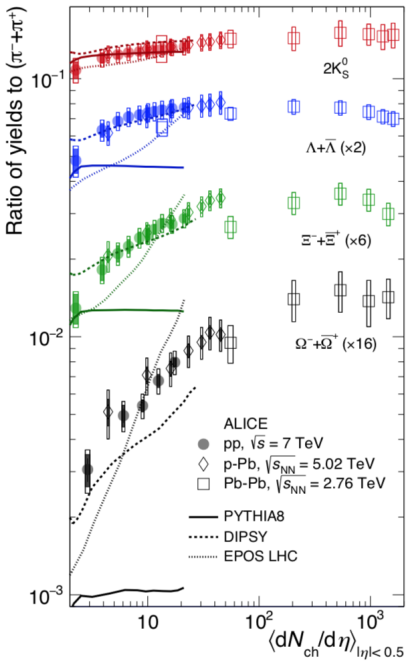

FIGURE 3.3: The yields of strange and multi-strange hadrons normalized to that of charged pions, as a function of particle multiplicity [**?**].

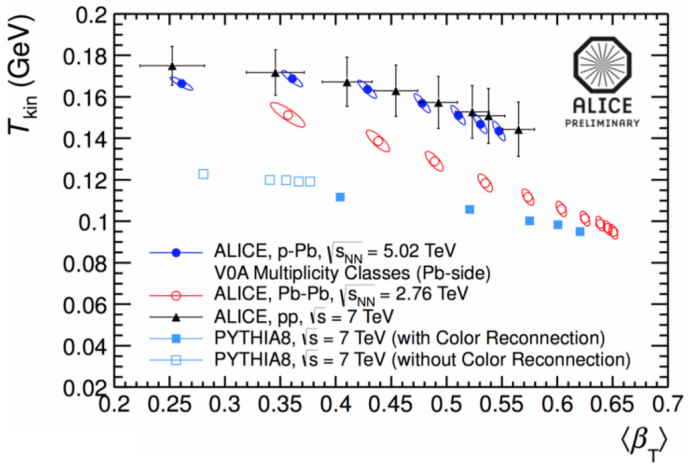

FIGURE 3.4: The comparison of BGBW fit parameters T^{fo}_{kin} - $< \beta_T >$ correlation for pp, p-Pb and Pb-Pb [39].

4 | Color Glass Condensate Scaling Variable

4.1 Expectations of $< p_T >$ Behavior as a Function of Collision Energy and Centrality

As mentioned before, in the CGC model, where the bulk properties at small x degrees of freedom are described by strong classical color fields, the gluon saturation is predicted at a corresponding saturation scale, Q_s. The local parton-hadron duality (LPHD) [40] picture is giving the dependence of the final multiplicities charged hadrons on the initial gluon fields, based on the assumption that the final multiplicities are proportional to the initial partonic one and considered to be independent of collision energy or centrality because the conversion of partons into hadrons takes place at a low virtuality scale, independent of the scale of the primary hard process.

If one assumes that in the LPHD framework, a gluon produces a number of n charged particles in the collision, after fragmentation, so the initial gluons would be described by [41, 42]:

$$\begin{aligned} < p_T >_g &\sim Q_s \\ \frac{1}{S_\perp}\frac{dN_g}{d\eta} &\sim Q_s^2 \end{aligned} \tag{4.1}$$

while for the final charged particles, due to the conservation of the transverse momentum during the fragmentation process, one gets:

$$\begin{aligned} < p_T >_{ch} &\sim \frac{Q_s}{n} \\ \frac{1}{S_\perp}\frac{dN_{ch}}{d\eta} &\sim nQ_s^2 \end{aligned} \tag{4.2}$$

which leads to:

$$\frac{< p_T >_{ch}}{\sqrt{\frac{1}{S_\perp}\frac{dN_{ch}}{d\eta}}} \sim \frac{1}{n\sqrt{n}} \tag{4.3}$$

In order to take into account the faster growth of multiplicity with the collision energy in A-A than in pp, one needs to consider that the number of charged hadrons produced in a gluon fragmentation is larger in A-A than in pp, which implies that the scaling values from Eq. 4.3 are smaller in central A-A collisions

than in pp, as is shown for RHIC data [14]. Since n increases with $< p_T >$, the $< p_T > /\sqrt{(dN/d\eta)/S_\perp}$ values should decrease with collision energy and centrality, behaviour that is not very clear in [14]. Based on the latest result obtained at RHIC within the BES program at low energies and the latest results obtained at LHC, such a dependence is worth to be reconsidered. In the next sections, the recipe used based on experimental data in order to extract the CGC inspired scaling variable, is presented.

4.2 dN/dy Estimates

Based on the correlation between the final state and the initial state from the LPHD picture, we have considered the total hadron density per unit of rapidity for the scaling variable, $\sqrt{(dN/dy)/S_\perp}$. The data used for light flavour hadrons, pions kaons and protons, were published in [14,43–45], while for hyperons the experimental data were published in [46–52].

For the BES program, the experimental values of the yields were not reported for $\sqrt{s_{NN}}$ = 19.6 and 27 GeV in the case of hyperons, so the values were extracted by interpolation, using energy dependence fits. Also, in the cases where some centralities were not reported, the corresponding values were obtained by interpolation using the centrality dependence fits. The yield values for Ω^- and $\bar{\Omega}^+$ were not reported for neither collision energy in the case of BES program, but from the extrapolation from the higher, available collision energies, to the BES ones, it has been shown that they have a negligible contribution, so the Ω^- and $\bar{\Omega}^+$ yields were neglected in the case of BES.

In order to estimate the final values of the total hadron density over unit of rapidity, we have used the following expression, based on the previously mentioned published experimental data:

For BES energies:

$$\frac{dN}{dy} \simeq \frac{3}{2}\frac{dN}{dy}^{(\pi^+ + \pi^-)} + 2\frac{dN}{dy}^{(K^+ + K^-, p+\bar{p}, \Xi^- + \bar{\Xi}^+)} + \frac{dN}{dy}^{(\Lambda + \bar{\Lambda})} \tag{4.4}$$

For $\sqrt{s_{NN}}$ = 62.4, 130 and 200 GeV:

$$\frac{dN}{dy} \simeq \frac{3}{2}\frac{dN}{dy}^{(\pi^+ + \pi^-)} + 2\frac{dN}{dy}^{(K^+ + K^-, p+\bar{p}, \Xi^- + \bar{\Xi}^+)} + \frac{dN}{dy}^{(\Lambda + \bar{\Lambda}, \Omega^- + \bar{\Omega}^+)} \tag{4.5}$$

For LHC energies:

$$\frac{dN}{dy} \simeq \frac{3}{2}\frac{dN}{dy}^{(\pi^+ + \pi^-)} + 2\frac{dN}{dy}^{(p+\bar{p}, \Xi^- + \bar{\Xi}^+)} + \frac{dN}{dy}^{(K^+ + K^-, K_s^0 + \bar{K}_s^0, \Lambda + \bar{\Lambda}, \Omega^- + \bar{\Omega}^+)} \tag{4.6}$$

For pp collisions at the LHC collision energy $\sqrt{s}$ = 7 TeV, the light flavour yields were estimated by integrating the p_T spectra from Ref. [39], while for hyperons, the ratio to pions given in Ref. [53] were extrapolated for higher multiplicites, so the following approximation was used:

$$\frac{dN}{dy} \simeq \frac{3}{2}\frac{dN}{dy}^{(\pi^+ + \pi^-)} + 2\frac{dN}{dy}^{(p+\bar{p},\Xi^- + \bar{\Xi}^+, K_s^0)} + \frac{dN}{dy}^{(K^+ + K^-, \Lambda + \bar{\Lambda}, \Omega^- + \bar{\Omega}^+)} \tag{4.7}$$

4.3 $S_\perp$ Estimates for A-A Collisions

As already mentioned in a previous section, the theoretical tool that is used to describe the geometry of a collision is the GMC framework. In this case, $S_\perp$ which represents the overlapping area between two colliding nuclei for a specific collision energy and centrality is estimated based on GMC approach. The nuclear density profile of the colliding nuclei is given in Eq. 2.1. Since w characterizes the deviations from a spherical shape, it is considered w=0 for each nucleus, so Eq. 2.1 becomes:

$$\rho(r) = \frac{1}{1 + exp(\frac{r - r_0}{a})} \tag{4.8}$$

with the corresponding input parameters for each nucleus: for the Au nucleus [14]: a = 0.535 fm,r_0 = 6.5 fm and for the Pb nucleus [43] a = 0.546 fm, r_0 = 6.62 fm.

Within the black disk approximation for nucleon-nucleon collisions, was used Eq. 2.3, for $\sigma_{inel}^{NN} = \sigma_{pp}$, with σ_{pp} as the nucleon-nucleon interaction cross section, for which the experimental data for the corresponding collision energies were taken from [14, 43, 54, 55]. All the information characterizing the collision were found in the literature: for BES program [44] (Au-Au collisions, with $\sqrt{s_{NN}}$ = 7.7, 11.5, 19.6, 27 and 39 GeV), for Au-Au at $\sqrt{s_{NN}}$ = 62.4, 130 and 200 GeV [14] and for Pb-Pb collisions at $\sqrt{s_{NN}}$ = 2.76 TeV [43] and $\sqrt{s_{NN}}$ = 5.02 TeV [45] at LHC.

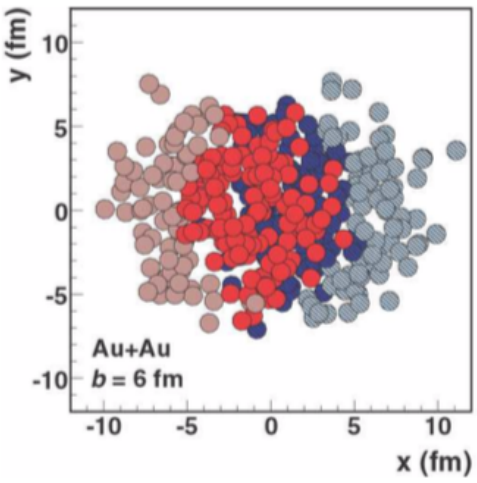

FIGURE 4.1: An example of a GMC simulation of a Au-Au collision at $\sqrt{s_{NN}}$ = 200 GeV, at a given impact parameter (b = 6 fm), viewed in the transverse plane; the nucleons of two colliding beams are represented with different colors (red and blue), while for the participating nucleons are used darker shades of red and blue [9].

The geometrical overlapping area ($S_{\perp}^{geom}$) were estimated by finding the maximum values of the x and y coordinates determined in an event (Fig. 4.1) and averaging them over many events. Another approach for the estimation of the overlapping areas is by taking into account the proportionality between $S_{\perp}^{var}$ and S (Eq. 4.9), where σ_x and σ_y are the variances of the participant distribution in the transverse plane, and σ_{xy} the covariance (Fig. 4.1), also averaged over many events. In the case of a complete overlap of the nuclei, the ratio between $S_{\perp}^{geom}$ and S is obtained and is used in order to rescale all the centrality dependent values. The results are presented in Fig. 4.2.

$$S = \sqrt{< \sigma_x >^2 < \sigma_y >^2 - < \sigma_{xy} >^2} \tag{4.9}$$

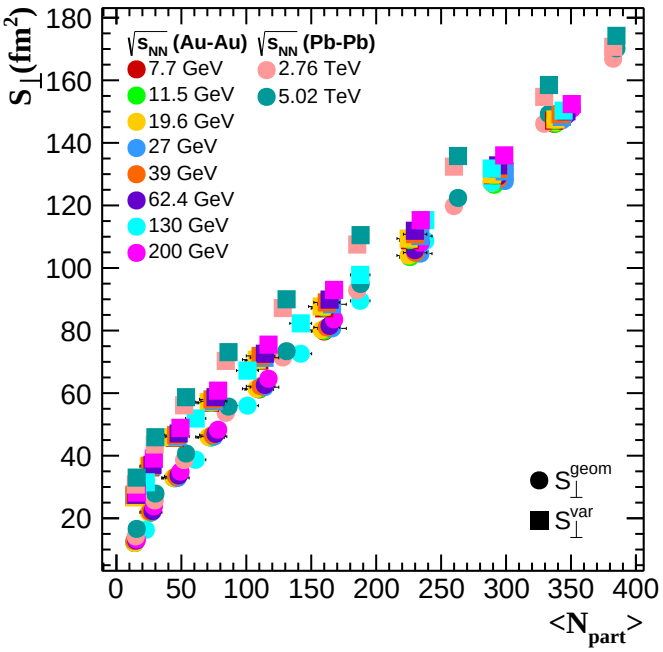

FIGURE 4.2: The overlapping area ($S_{\perp}$) estimated within the GMC approach as a function of the average number of participants ($< N_{part} >$) for different collision energies and centralities (full dots: $S_{\perp}^{geom}$; full squares: $S_{\perp}^{var}$) [56].

4.4 $S_{\perp}$ Estimates for pp Collisions

As already mentioned, the GMC approach is no longer accurate to describe the geometry in pp collision, thus, the overlapping area for pp collisions ($S_{\perp}^{pp} = \pi R_{pp}^2$) cannot be estimated similar as in A-A collisions. In order to estimate $S_{\perp}^{pp}$, the IP-Glasma initial state model framework was used [57,58]. This approach allows the estimation

of the maximal radius for which the energy density of the Yang-Mill fields is larger than:

$$\varepsilon = \alpha \Lambda_{QCD}^4 \tag{4.10}$$

The α values cannot be precisely estimated, but it's limits are known: $\alpha \in [1, 10]$, and the maximal radius for pp collisions is estimated in Ref. [57] for both $\alpha = 1$ and $\alpha = 10$, as a function of the total number of gluons in the initial state, powered by (1/3) (Fig. 4.3).

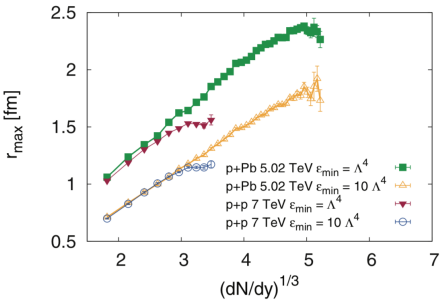

FIGURE 4.3: The maximal radius estimated within the IP-Glasma initial state model, as a function of the total number of gluons in the initial state to the power of 1/3 [57].

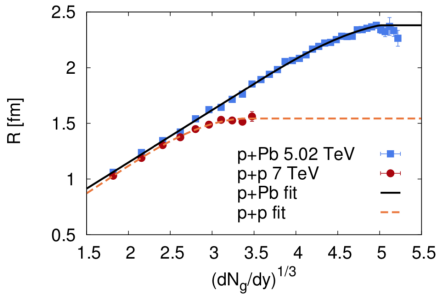

FIGURE 4.4: The maximal radius dependence on the number of gluons to the power of 1/3 taken from Ref. [57] for α = 1, fitted with the function given in Eq. 4.11 [58].

In Ref. [58], the r_{max} values were taken from Ref. [57] for $\alpha = 1$ and fitted with the following function (Fig. 4.4):

$$f_{pp} = \begin{cases} 0.387 + 0.0335x + 0.274x^2 - 0.0542x^3 & \text{if } x < 3.4, \\ 1.538 & \text{if } x \geq 3.4. \end{cases} \tag{4.11}$$

In order to be consistent and take into account all the possible values that α can have, we have also analysed the $\alpha = 10$ upper limit, so, based on the same recipe given in Ref. [58], we have fitted the r_{max} values given in Ref. [57] for $\alpha = 10$ (Fig. 4.3) with the following expression:

$$f_{pp} = \begin{cases} -0.018 + 0.3976x + 0.095x^2 - 0.028x^3 & \text{if } x < 3.4, \\ 1.17 & \text{if } x \geq 3.4. \end{cases} \tag{4.12}$$

where $x = (dN_g/dy)^{1/3}$. The gluon density per unit of rapidity was approximated by: $dN_g/dy \approx dN/dy$ and the total hadron density per unit of rapidity was obtained based on Eq. 4.7.

The final values of the CGC inspired scaling variable, $\sqrt{(dN/dy)/S_\perp^{geom}}$ as a function of collision energies, for different centralities (A-A) and multiplicity classes (pp) are displayed in Fig. 4.5.

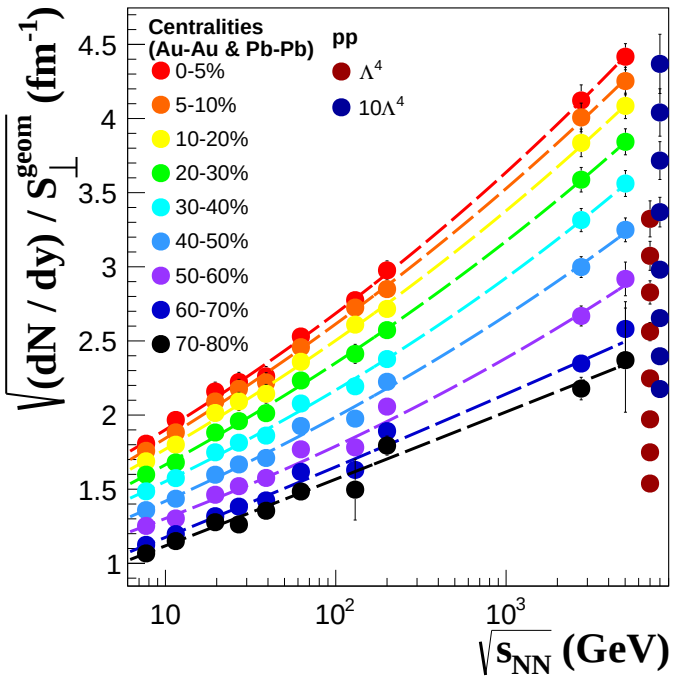

FIGURE 4.5: The scaling variable, $\sqrt{(dN/dy)/S_{\perp}^{geom}}$, as a function of $\sqrt{s_{NN}}$ for different centralities and multiplicity classes. The dashed lines represent the fits performed using a power-law function for each centrality. In the case of pp collisions, the values are displayed for both values of the α parameter ($\alpha = 1$ dark red markers, $\alpha = 10$ dark blue markers). For a better visualisation of these results, the dark blue markers are artificially displaced in $\sqrt{s_{NN}}$ [56].

5 | Results

As mentioned in the previous chapter, the assumptions made using the LPHD approach and the correlation between the initial and final states, are giving the dependence of $< p_T > / \sqrt{(dN/dy)/S_{\perp}^{geom}}$ from Eq. 4.3 as a function of the number of the charged hadron produced in a gluon fragmentation. It is necessary to mention that the LPHD framework doesn't take into account any collective effects, so the $< p_T >$ is expected to decrease with the increase of the collision energy and with centrality. In this study, this dependence is studied for a wide range of energies (from 7.7 GeV up to 5.44 TeV) and for different colliding systems (Au-Au, Cu-Cu, Pb-Pb and Xe-Xe).

Based on the previous mentioned similarities between pp and A-A collisions, a systematic study between pp and Pb-Pb system at LHC energies of this scaling was also performed.

5.1 Systematic Study of the $\sqrt{s_{NN}}$ Dependence

5.1.1 $< p_T >$ as a function of $\sqrt{(\frac{dN}{dy})/S_{\perp}^{geom}}$

In this section the results on the dependence of the $< p_T >$ on the scaling variable are presented. The $< p_T >$ for Au-Au collisions at the corresponding energies for the BES program ($\sqrt{s_{NN}}$ = 7.7, 11.5, 19.6, 27 and 39 GeV) [44], for $\sqrt{s_{NN}}$ = 62.4, 130 and 200 GeV [14] and for Pb-Pb collisions at the LHC energies of $\sqrt{s_{NN}}$ = 2.76 TeV and 5.02 TeV [43, 45] for positive pions, kaons and protons (π^+, K^+ and p) are presented in Fig. 5.1 for both the estimations used for the $S_{\perp}$ values (*Fig. 5.1 (a)*: $S_{\perp}^{geom}$ and *Fig. 5.1 (b)*: $S_{\perp}^{var}$).

The experimental values were fitted with a first-order polynomial function, for each collision energy. As one can notice, the quality of the fits presented in the bottom plots of both Fig. 5.1 (a) and Fig. 5.1 (b) in term of Data/Fit ratio are equally good. The scaling works very good for all the RHIC energies, but between the results obtained in the collision energies at RHIC ($\sqrt{s_{NN}}$ = 200 GeV) and the LHC energies, a clear offset can be observed.

The data/fit plots are showing a linear dependence of $< p_T >$ on the scaling variable, the ratio being almost one for all the available energies, within the errors bars. Nevertheless, a very interesting feature can be observed for the LHC energies,

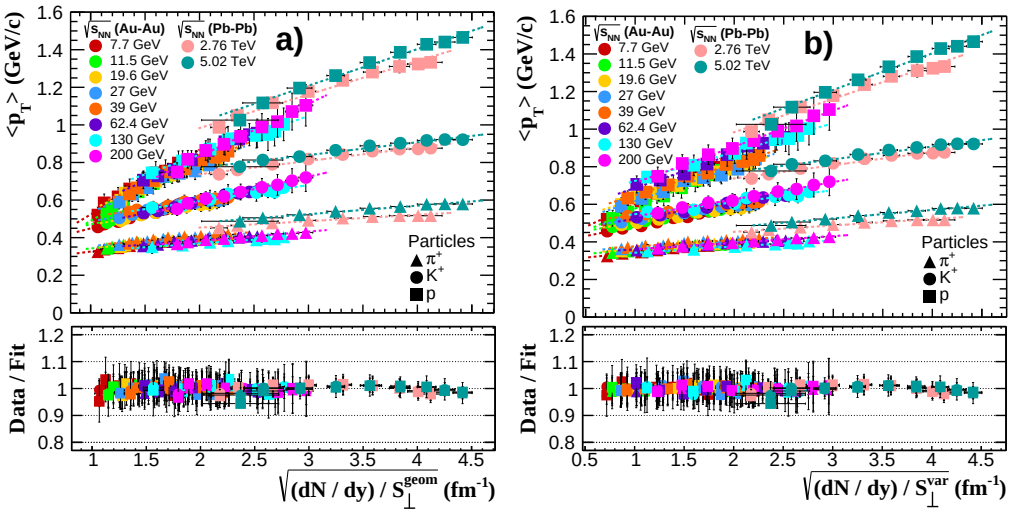

FIGURE 5.1: **(a)** *Top*: The $< p_T >$ of positive pions, kaons and protons as a function of the scaling variable, $\sqrt{(dN/dy)/S_\perp^{geom}}$, for all the measured energies and centralities in Au-Au at RHIC [14, 44] and Pb-Pb at LHC [43, 45]. The dashed lines represent the fits for each $\sqrt{s_{NN}}$ with a first order polynomial function; *Bottom:* The ratio between the experimental values and the values of a linear fit for each centrality and collision energy, in order to characterize the quality of the fits. **(b)** The same as for (a), but for $\sqrt{(dN/dy)/S_\perp^{var}}$ [56].

where there is present a deviation from the general trend for the most central collisions, which can be interpreted as a sign of gluon saturation. However, this feature has to be carefully further investigated.

The parameters of the linear fits from Fig. 5.1 are presented in Fig. 5.2, in terms of the slope (Fig. 5.2 (a)) and of the offset (Fig. 5.2 (b)). As one can notice, the slope values are increasing form pions to protons. Even though the errors bars are rather large for BES energies, a systematic decrease of the slope ($< p_T > / \sqrt{(dN/dy)/S_\perp^{geom}}$) is observed (full symbols, continuous line), as theory predicts. This trend seems to be mass dependent, since it becomes more proeminent from pions to protons. In terms of $S_\perp^{var}$ (open symbols, dashed line), the slope is clearly smaller at lower collision energies. To better observe the dependence of the slope on the collision energy, the data points were fitted with the following function:

$$f(x) = a + \frac{b}{ln(x)} \tag{5.1}$$

In terms of the offsets (Fig. 5.2 (b)), their values are similar for all the RHIC energies (from 7.7 GeV up to 200 GeV) and are systematically increasing for the LHC energies (2.76 and 5.02 TeV) for all the three species, for both $S_\perp^{geom}$ and $S_\perp^{var}$. The results obtained with the use of $S_\perp^{var}$ are similar to those obtained from $S_\perp^{geom}$ within the error bars for pions and kaons, while for protons can be observed a systematically growth of the offset values at RHIC energies. It is worth mentioning that for LHC

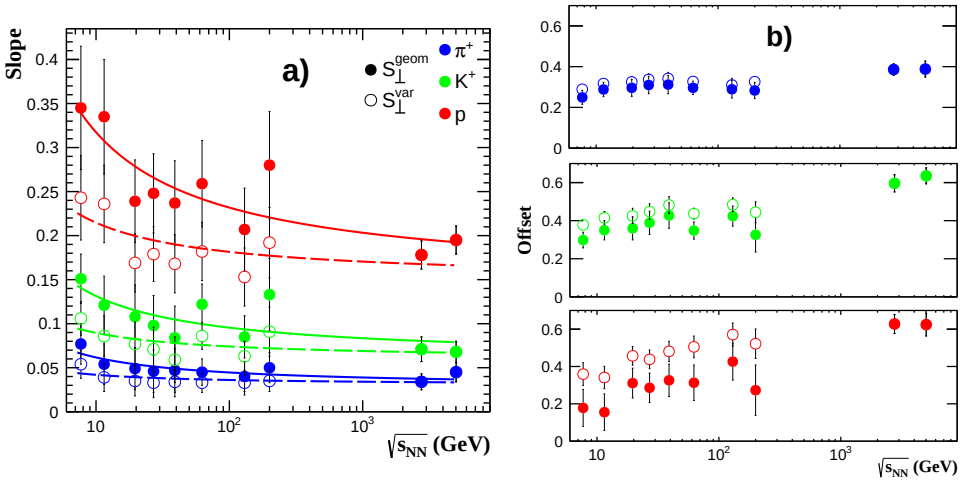

FIGURE 5.2: **(a)** The slope of the $< p_T >= f(\sqrt{(dN/dy)/S_\perp})$ (Fig. 5.1) for $\sqrt{(dN/dy)/S_\perp^{geom}})$ (full symbols) and for $\sqrt{(dN/dy)/S_\perp^{var}})$ (open symbols). The slope dependence on the collision energy, $\sqrt{s_{NN}}$ is fitted with the function given in Eq. 5.1 ($S_\perp^{geom}$ - continuous line; $S_\perp^{var}$ - dashed line), separately for pions (blue markers), kaons (green markers) and protons (red markers); **(b)** The offsets of the $< p_T >= f(\sqrt{(dN/dy)/S_\perp})$ (Fig. 5.1) as a function of collision energy, separately for pions (top), kaons (center) and protons (bottom) [56].

energies, the values of both the slopes and offsets are the same when using $S_\perp^{geom}$ and $S_\perp^{var}$. Since the observed trends are rather similar in both cases of $S_\perp = S_\perp^{geom}$ and $S_\perp = S_\perp^{var}$, the results will be presented only in terms of $S_\perp^{geom}$.

Core-Corona Interplay

In order to see in which extent the saturation trend observed in the most central collisions at the LHC energies are due to the core-corona interplay and how does the $< p_T >= f(\sqrt{(dN/dy)/S_\perp})$ dependence look like for the core contribution, a further investigation in terms of core-corona interplay was performed. For $\sqrt{s_{NN}}$ = 200 GeV (Au-Au collisions) and for $\sqrt{s_{NN}}$ = 2.76 and 5.02 TeV (Pb-Pb collisions) we estimated the core contributions in terms of mean transverse momentum ($< p_T >^{core}$) and scaling variable ($\sqrt{(dN/dy)^{core}/(S_\perp^{geom})^{core}}$) based on the recipe given in Ref. [13] and previously described in Section 2.3. The $< p_T >^{corona}$ and $(dN/dy)^{corona}$ values were measured in pp^{MB} collisions, reported in Ref. [14] for $\sqrt{s_{NN}}$ = 200 GeV, by the STAR Collaboration, while for $\sqrt{s_{NN}}$ = 2.76 and 5.02 TeV the experimental values for minimum bias pp collisions were reported in Refs. [59, 60] by the ALICE Collaboration.

A comparison between the experimental values and the corresponding values of the extracted core contribution is presented in Fig. 5.3. In order to extract some quantitative information about the different trends of all experimental vs. core $< p_T >$

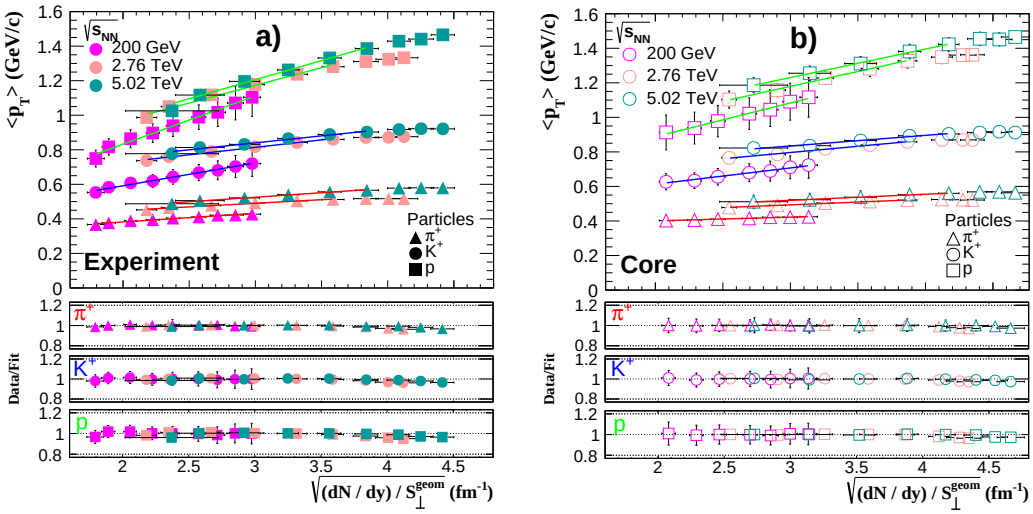

FIGURE 5.3: **(a)** *Top:* The $< p_T >$ experimental values for π^+, K^+ and p, as a function of the scaling variable, fitted with a first order polynomial function, separately for pions, kaons and protons; *Bottom:* The quality of the fits in terms of data/fit ratio for each specie. **(b)** Same as in (a), but for the extracted core contributions [56].

values, a linear fit was performed for all particle species. As mentioned before, for $\sqrt{s_{NN}}$ = 2.76 and 5.02 TeV the last three points, that correspond to the most central collisions, systematically deviate from the general trend and therefore were excluded from the fits. These deviations from the general trends can also be observed in the bottom plots of Fig. 5.3, where the fit qualities are represented. The fit results in terms of slopes are presented In Table 5.1. As one can observe, even if the qualities of the fit are similar for the experimental values and for the core contribution, the slope values for the core contribution are systematically smaller than of those corresponding to experimental values (Table 5.1) and the difference between the LHC energies and the highest RHIC energy is reduced. However, the saturation observed for the most central collisions at the LHC energies can still be observed.

$\sqrt{s_{NN}}$ (GeV)	Experiment			Core		
	π^+	K^+	p	π^+	K^+	p
200	0.05 ± 0.02	0.13 ± 0.04	0.28 ± 0.06	0.02 ± 0.03	0.09 ± 0.06	0.20 ± 0.11
2760	0.04 ± 0.01	0.09 ± 0.02	0.20 ± 0.03	0.03 ± 0.02	0.07 ± 0.03	0.17 ± 0.04
5020	0.05 ± 0.02	0.08 ± 0.02	0.22 ± 0.03	0.03 ± 0.03	0.06 ± 0.02	0.17 ± 0.04

TABLE 5.1: The slopes of the linear fit of the $< p_T >$ as a function of $\sqrt{(dN/dy)/S_\perp}$, for pions, kaons and protons corresponding to $\sqrt{s_{NN}}$ = 200 GeV, 2.76 TeV and 5.02 TeV, separately for experimental values and the core contribution. The three points corresponding to the most central collisions at LHC energies ($\sqrt{s_{NN}}$ = 2.76 and 5.02 TeV) were not included in the fit [56].

5.1.2 $< p_T >$ mass dependence as a function of $\sqrt{(\frac{dN}{dy})/S_{\perp}^{geom}}$

The slope of the $< p_T >$ dependence on particles mass (pions, kaons and protons) can give an insight on the dynamics of the collision, if one takes into account the basic definition of the momentum of a particle with mass. The $< p_T >$ = f(mass) dependences are linear for each centrality, except for the most peripheral ones, so fits with linear functions were performed for these dependences, for all collision energies and centralities. The parameters of this fits are represented in Fig. 5.4 ((a)-particles; (b)-antiparticles) in terms of the slopes of these fits, while in Fig. 5.5 ((a)-particles; (b)-antiparticles) are represented the corresponding offsets.

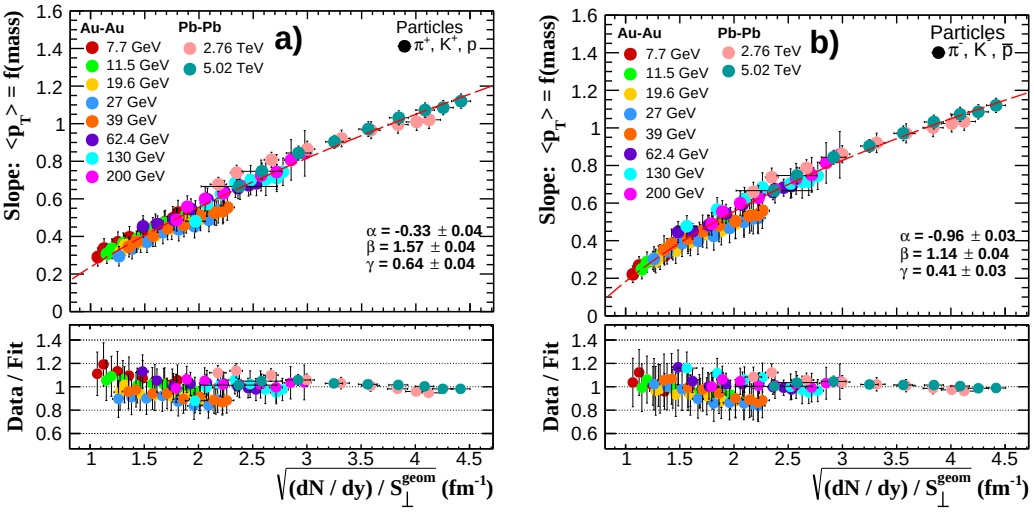

FIGURE 5.4: **(a)** *Top:* The slopes of the $< p_T >= f(mass)$ dependence for π^+, K^+ and p, as a function of the scaling variable, fitted with the expression given in Eq. 5.2, with the parameters listed in the figure; *Bottom:* The quality of the fits in terms of data/fit ratio. **(b)** Same as in (a), but for the associated antiparticles (π^-, K^- and $\bar{p}$) [56].

The slope dependencies on the scaling variable from Fig. 5.4 are fitted with the expression given in Eq. 5.2 and the fit parameters are also displayed in Fig. 5.4. As one can observe, in terms of the slope of $< p_T >= f(mass)$ dependence (Fig. 5.4) a very good scaling was obtained for both particles (Fig. 5.4 (a)) and antiparticles (Fig. 5.4 (b)), that follows the trend of Eq. 5.2 very closely, within the error bars, except for $\sqrt{s_{NN}}$ = 19.6, 27 and 39 GeV, for which the slopes are slightly deviating from the general trends. The quality of the fits is presented in the bottom plots, in terms of data/fit ratio.

$$Slope_{<p_T>=f(mass)} = \alpha + \beta(\sqrt{(dN/dy)/S_{\perp}^{geom}})^{\gamma} \tag{5.2}$$

The corresponding offsets of the $< p_T >= f(mass)$ dependence are represented in Fig. 5.5, separately for particles (Fig. 5.5 (a)) and antiparticles (Fig. 5.5 (b)). Even if the error bars are rather large, for the LHC energies there can be observed almost

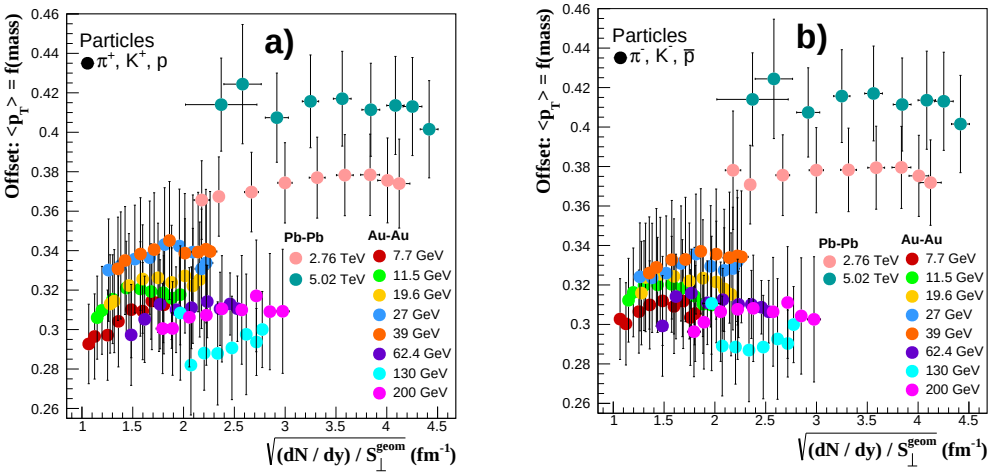

FIGURE 5.5: **(a)** The offsets of the $< p_T >= f(mass)$ dependence for π^+, K^+ and p, as a function of the scaling variable; **(b)** Same as in (a), but for the associated antiparticles (π^-, K^- and $\bar{p}$) [56].

a constant value, while for collision energies up to 62.4 GeV, a systematic increase is observed for $\sqrt{(dN/dy)/S_{\perp}^{geom}} < 1.7 fm^{-1}$.

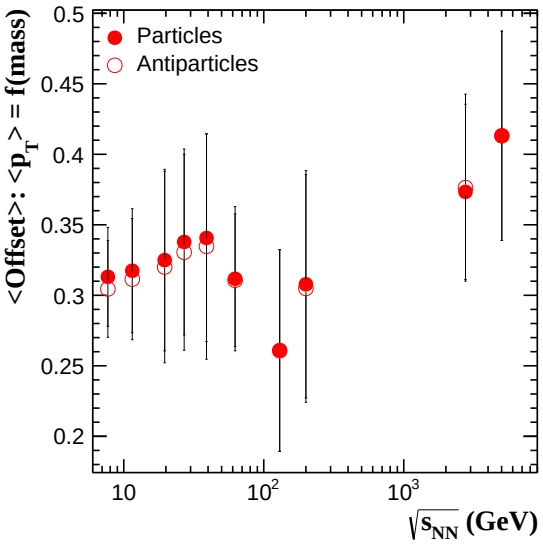

FIGURE 5.6: The average values of the $< p_T >= f(mass)$ offsets, corresponding to $\sqrt{(dN/dy)/S_{\perp}^{geom}} \geq 1.7\ fm^{-1}$ as a function of collision energy, $\sqrt{s_{NN}}$, for particles (π^+, K^+, p - full symbols) and antiparticles (π^-, K^-, $\bar{p}$ - open symbols) [56].

For values of $\sqrt{(dN/dy)/S_{\perp}^{geom}}$ larger than 1.7 fm^{-1} a plateau is reached for all the collision energies. In order to observe a $\sqrt{s_{NN}}$ dependence, we have averaged for each collision energy only the offset values corresponding to $\sqrt{(dN/dy)/S_{\perp}^{geom}} \geq 1.7\ fm^{-1}$. The results obtained are represented in Fig. 5.6, for both particles (full symbols) and antiparticles (open symbols).

5.1.3 $\sqrt{(\frac{dN}{dy})/S_{\perp}^{geom}}$ dependence of Boltzmann-Gibbs Blast Wave Fit parameters

The Boltzmann Gibbs blast wave (BGBW) expression (Eq. 5.3), inspired from hydrodynamical models [28] which make phenomenological assumptions that the particles produced in a system are locally thermalized at a kinetic freeze-out temperature and they develop a collective behavior, moving with a collective transverse flow velocity, that is common for all the particles involved. At this stage of the collision, the particles can be considered as a fireball, that is modelled under the assumption that it has an azimuthally isotropic shape, characterized by a kinetic freeze-out temperature (T_{kin}^{fo}) and a transverse flow velocity (β_T). The BGBW expression (Eq. 5.3) gives a very good description of particles spectra, by taking into account these collective effects.

$$\frac{dN}{p_T dp_T} \propto \int_0^R r dr m_T I_0(\frac{p_T sinh(\rho)}{T_{kin}^{fo}}) K_1(\frac{m_T cosh(\rho)}{T_{kin}^{fo}}) \tag{5.3}$$

with

$$\begin{aligned} \rho &= tanh^{-1}(\beta_T) \\ m_T &= \sqrt{p_T^2 + m_0^2} \\ \beta_T(r) &= \beta_s(\frac{r}{R})^n \end{aligned} \tag{5.4}$$

where I_0 and K_1 represent the modified Bessel functions, β_s is the surface velocity, (r/R) is the relative radial position in the fireball and n defines the expansion profile.

In order to extract the freeze-out properties of the collision from the available data, the p_T spectra of π^+, K^+ and p and those of their corresponding antiparticles (π^-, K^-, $\bar{p}$) were fitted simultaneously with the BGBW expression (Eq. 5.3), with three free parameters: β_s, T_{kin}^{fo} and n. The mean values of the transverse flow velocity, $< \beta_T >$, were found using the expression given in Eq. 5.5. All the available data for $< \beta_T >$ [14, 43–45, 61] as a function of the scaling variable, are presented in Fig. 5.7.

$$< \beta_T >= \frac{2}{2+n}\beta_s \tag{5.5}$$

Another aspects that one has to consider are the differences between particles and antiparticles p_T spectra, that become more prominent with the decrease of the collision energy, $\sqrt{s_{NN}}$. In order to see in which extent the particles and antiparticles behave differently, for some energies and centralities where azimuthal dependent BGBW fits were performed [62, 63], the $< \beta_T >$ values for antiparticles were plotted in Fig. 5.7 (open symbols), while the full symbols represent the case when p_T

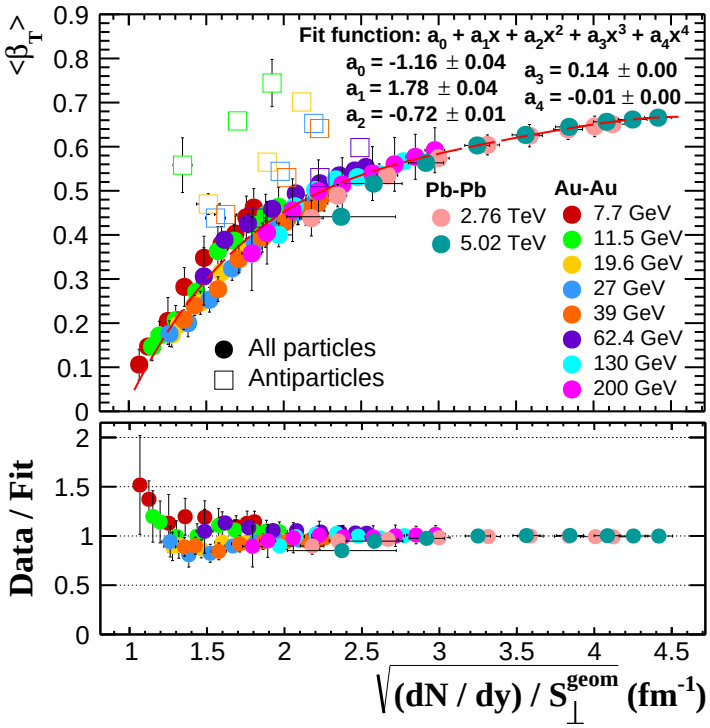

FIGURE 5.7: *Top:* The BGBW fit parameter $< \beta_T >$ values as a function of the scaling variable, $\sqrt{(dN/dy)/S_{\perp}^{geom}}$, taking into account only the antiparticles (open symbols) and all the particles (full symbols) - fitted with a 4^{th} order polynomial function; *Bottom:* The quality of the fit as data/fit ratio [56].

spectra of all particles (both particles and antiparticles) are fitted with the BGBW expression simultaneously. One can observe in Fig. 5.7 that the differences between these two cases are less and less significant with increasing the collision energy, being very prominent for $\sqrt{s_{NN}}$ = 11.5 GeV and almost negligible for $\sqrt{s_{NN}}$ = 62.4 GeV, so it becomes very important that one takes into account separately the contributions of particles and antiparticles, since at low energies there are more particles produced in the collision than antiparticles, the contribution in the observed trends being almost entirely dominated by particles. In Fig. 5.7, one can observe that for the published $< \beta_T >$ values, a very good scaling as a function of the scaling variable ($\sqrt{(dN/dy)/S_{\perp}^{geom}}$) was obtained, described rather good by a 4^{th} order polynomial function that was used as a fit function for all energies and centralities (the parameters of the fit function are displayed in Fig. 5.7). In the bottom plot, the fit quality is displayed as data/fit ratio, where one can observe that for all the collision energies the data scale rather good, except for the most peripheral collisions corresponding to the lowest BES available energies ($\sqrt{s_{NN}}$ = 7.7 and 11.5 GeV).

The dynamics of the $< \beta_T >$ BGBW parameter can be observed in Fig. 5.8 where

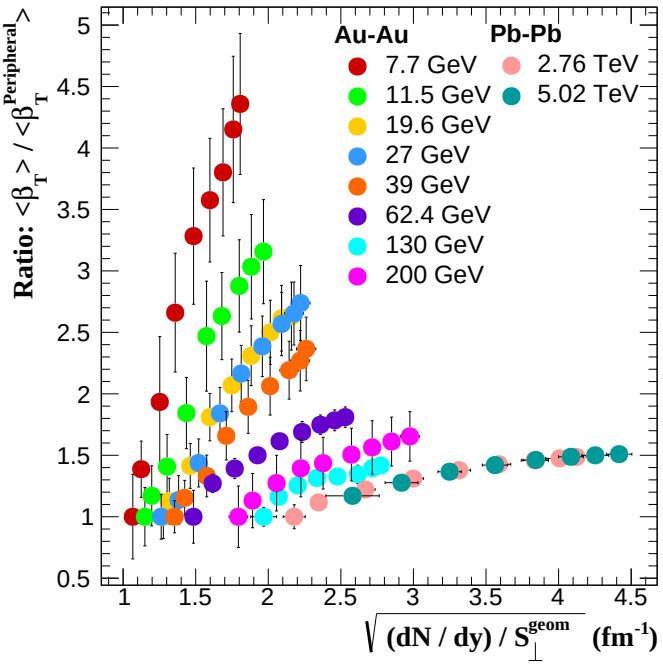

FIGURE 5.8: The ratio between the $< \beta_T >$ values and the ones corresponding the the most peripheral collisions, as a function of the scaling variable, $\sqrt{(dN/dy)/S_{\perp}^{geom}}$ [56].

values of $< \beta_T >$ corresponding to each centrality were divided to the most peripheral (58-85% for $\sqrt{s_{NN}}$ = 130 GeV and 70-80% for all the other collision energies) $< \beta_T >$ values, at the corresponding collision energy. The values oh the $< \beta_T > / < \beta_T >^{Peripheral}$ ratio are plotted in Fig. 5.8 as a function of $\sqrt{(dN/dy)/S_{\perp}^{geom}}$.

In Fig. 5.9, the data for the kinetic freeze-out temperature (T_{kin}^{fo}) and for the expansion profile parameter, n [14, 43–45, 61] as a function of the scaling variable, $\sqrt{(dN/dy)/S_{\perp}^{geom}}$, are presented. Due to rather large errors bars, one could conclude only on a global trend, i.e. for the RHIC values ($\sqrt{s_{NN}}$ = 7.7 up to 200 GeV) the T_{kin}^{fo} show an almost linear decrease, while a shift of almost 20 MeV is observed when moving from the highest energy available at RHIC to LHC energies, as for the $< p_T >$ dependence (Fig. 5.1) or for the offset of $< p_T >$ = f (mass) dependence (Fig. 5.5). From Fig. 5.9 (b), is not evidenced only systematic energy dependence of the n BGBW fit parameter, the parameter's values being scattered, with an opposite trend for $\sqrt{s_{NN}}$ = 62.4 and 200 GeV than for the LHC energies. It is very important to have in mind that different fit ranges were used in the literature [14, 43–45, 61] for the BGBW fit expression, so the consistency of this study may be affected. The different p_T ranges used for the fit expression are selected in order to reduce as much as possible the contributions of other processes, like resonance decays in the case of

low p_T pions, or suppression effects for higher p_T values for all particle species.

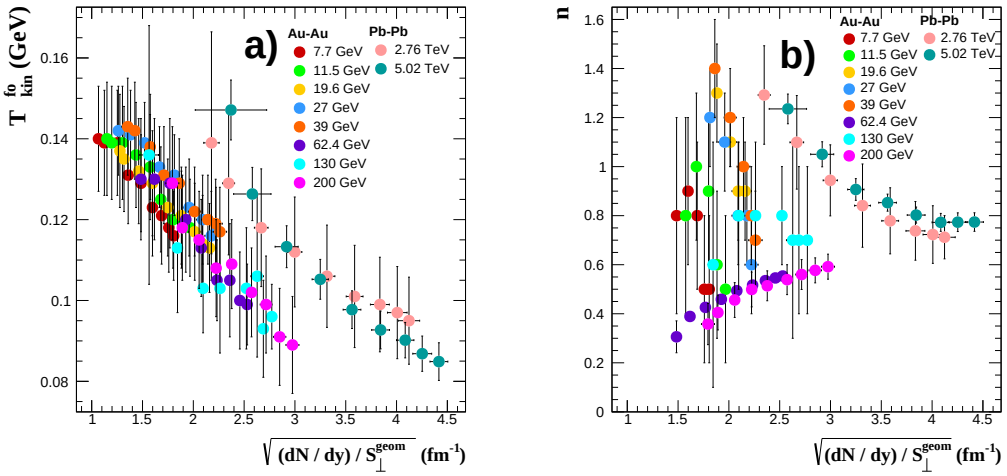

FIGURE 5.9: **(a)** The T^{fo}_{kin} BGBW fit parameter as a function of the geometric variable, $\sqrt{(dN/dy)/S^{geom}_{\perp}}$; **(b)** Same as in (a), but for the n parameter [56].

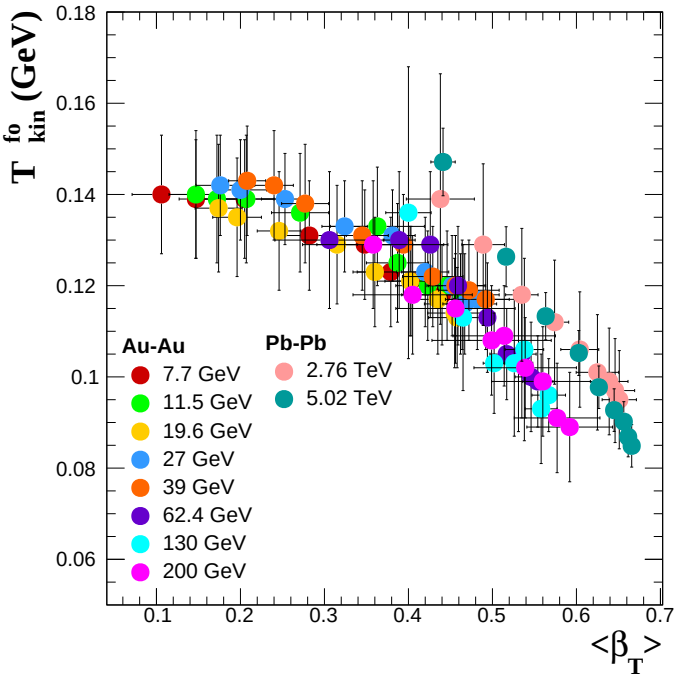

FIGURE 5.10: The T^{fo}_{kin} BGBW fit parameter dependence on $< \beta_T >$ [56].

In Fig. 5.10 the kinetic freeze-out temperature BGBW fit parameter is plotted as a function of the average transverse flow velocity (T_{kin}^{fo} = f($< \beta_T >$)). A systematic scaling is observed for all the RHIC energies, while the same shift can be observed between the highest RHIC energy and the LHC energies.

5.2 Systematic Study of the System Size Dependence

5.2.1 Heavy Ion Collisions

In order to take into account the role played by the system size in this CGC inspired scaling, we have compared several colliding systems for the same or with a slightly different collision energy. In this study we have compared the Cu-Cu and Au-Au collision systems, both measured at $\sqrt{s_{NN}}$ = 200 GeV at RHIC, but we have also extended this study to heavier systems at a much higher collision energy, like Pb-Pb and Xe-Xe, at $\sqrt{s_{NN}}$ = 5.02 TeV and 5.44 TeV, respectively. The scaling variable for these new systems was estimated as described in Chapter 4, with data for Xe-Xe available in Refs. [64, 65] and for Cu-Cu available in Refs. [66, 67].

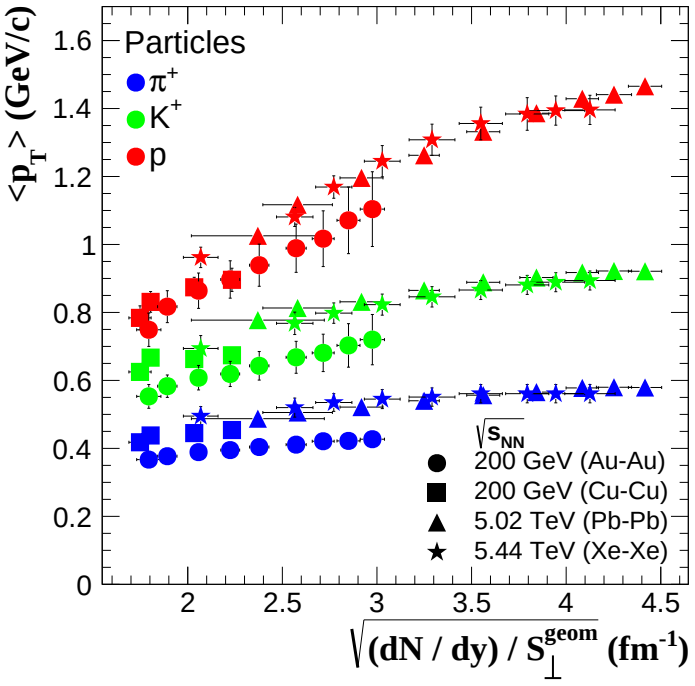

FIGURE 5.11: The $< p_T >$ dependence on the scaling variable, $\sqrt{(dN/dy)/S_{\perp}^{geom}}$, for positive pions (blue markers), kaons (green markers) and protons (red markers), for different colliding systems and energies [68].

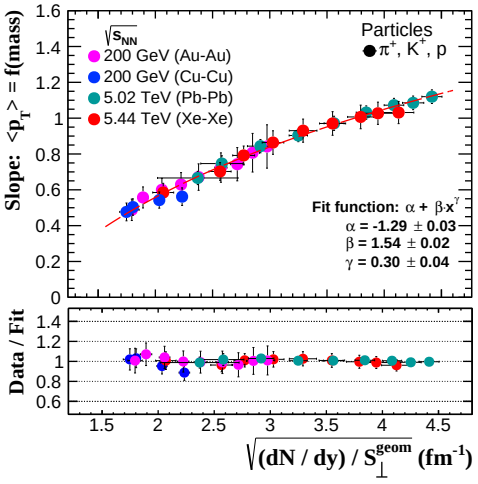

FIGURE 5.12: *Top:* The slope of $< p_T >$ = f(mass) as a function of the scaling variable, $\sqrt{(dN/dy)/S_{\perp}^{geom}}$, fitted with the expression given in Eq. 5.2, for different colliding systems and energies; *Bottom:* The quality of the fit in terms of data/fit ratio [68].

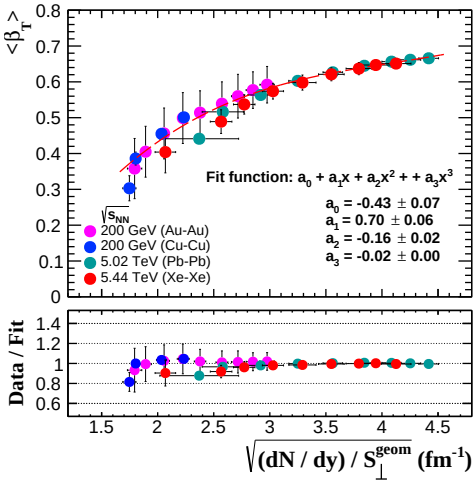

FIGURE 5.13: *Top:* The average values of the BGBW fit parameter, $< \beta_T >$, as a function of the scaling variable, $\sqrt{(dN/dy)/S_{\perp}^{geom}}$, fitted with a 3^{rd} order polynomial function, for different colliding systems and energies; *Bottom:* The quality of the fit in terms of data/fit ratio [68].

In Fig. 5.11, one can observe a very good scaling between the LHC energies, for similar collision energies: Pb-Pb at $\sqrt{s_{NN}}$ = 5.02 TeV and Xe-Xe at $\sqrt{s_{NN}}$ = 5.44 TeV. When moving to much lower collision energies at RHIC ($\sqrt{s_{NN}}$ = 200 GeV) and different symmetric systems (Au-Au and Cu-Cu), a shift to larger values is observed for Cu-Cu, relative to Au-Au, the shift decreasing from pions to protons. When comparing all these collision systems at different energies, one can notice a shift between RHIC and LHC energies.

In terms of the slope of the $< p_T >$ as a function of mass of pions, kaons and protons (Fig. 5.12) and for the average values of the BGBW fit parameter, $< \beta_T >$ (Fig. 5.13) as a function of scaling variable, $\sqrt{(dN/dy)/S_{\perp}^{geom}}$, one can observe a very good scaling for all the different symmetric systems (Cu-Cu: blue markers; Au-Au: magenta markers; Xe-Xe: red markers and Pb-Pb: green markers) and energies. The slopes of $< p_T >$ = f(mass) dependences on the scaling variable were fitted with the expression given in Eq. 5.2, with the parameters displayed in Fig. 5.12, while the BGBW fit parameter's dependence on $\sqrt{(dN/dy)/S_{\perp}^{geom}}$ was fitted with a third-order polynomial function, with parameters displayed in Fig. 5.13. The qualities of the fits are displayed in the bottom plots of each figure.

5.2.2 Small systems (pp) versus heavy systems (Pb-Pb) at LHC energies

As previously mentioned, since several similarities were observed between pp and Pb-Pb systems, the small systems have started to play a major interest by themselves, and not only as heavy-ion collisions references. The results presented in this section

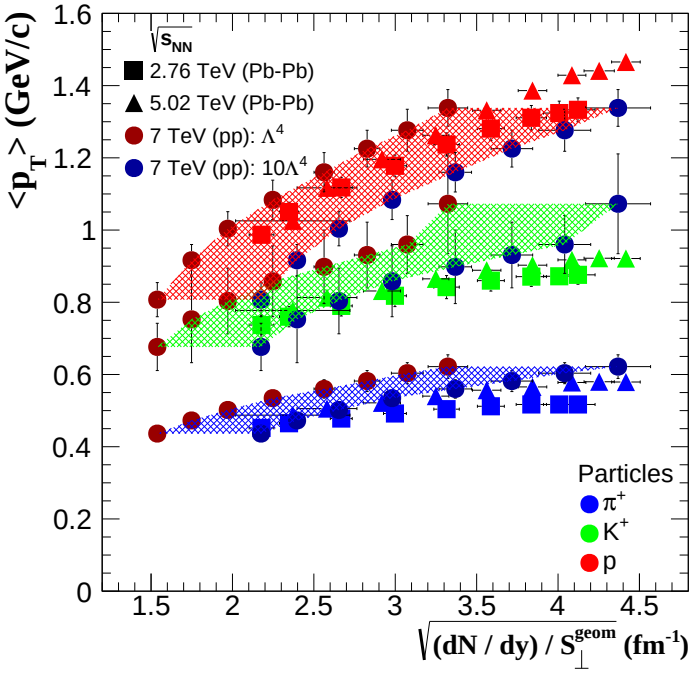

FIGURE 5.14: The $< p_T >$ as a function of scaling variable, for positive pions, kaons and protons, for Pb-Pb ($\sqrt{s_{NN}}$ = 2.76 TeV (squares) and 5.02 TeV (triangles)) and pp (α = 1: dark red markers; α = 10: dark blue markers) [56].

were obtained in order to see how this scaling can reveal similarities between pp ($\sqrt{s}$ = 7 TeV) and Pb-Pb ($\sqrt{s_{NN}}$ = 2.76 and 5.02 TeV) colliding systems, in terms of the already mentioned observables ($< p_T >$, the slope of $< p_T >$ = f(mass) and $< \beta_T >$). The recipes used in order to obtain the scaling variable is presented in Chapter 4, for both pp and Pb-Pb systems. In order to be consistent, in the pp case, since the overlapping area has two limits, for α = 1 and for α = 10, and the values of α can't be precisely known ($\alpha \in [1, 10]$), the scaling variable was estimated for both values, the results in between (α = 1: dark red markers; α = 10: dark blue markers) being represented by a shaded area.

In the pp case, the $< p_T >$ values were obtained by fitting the published p_T spectra [39] with the following expression [69]:

$$\frac{d\sigma}{p_T dp_T} = A_e exp(\frac{-E_T^{kin}}{T_e}) + \frac{A}{(1 + \frac{p_T^2}{T^2 n})^n} \tag{5.6}$$

which was found to best describe the experimental data.

In Fig. 5.14 the comparison between pp and Pb-Pb at LHC energies is presented, in terms of the dependence of the $< p_T >$ on the scaling variable. As one can observe, a general trend seems to set in for both pp and Pb-Pb systems, for all the three

species, and there are several reasons for which a scaling we have actually obtained, like the $< p_T >$ enhancement for kaons in pp relative to Pb-Pb, the difference in terms of collision energies, or the large inhomogeneity of the initial state in the pp case, which directly affects the estimation of $S_\perp$ and also the suppression present in Pb-Pb and not evidenced in pp collisions, yet.

In terms of slope (Fig. 5.15) of the $< p_T >$ as a function of mass of pions, kaons and protons, and of the average values of the BGBW fit parameter, $< \beta_T >$ (Fig. 5.16), obtained from the simultaneous fits of p_T spectra of charged pions, kaons and protons (both particles and antiparticles) a very good scaling with Pb-Pb can be observed for α = 1, which was considered the most adequate value for the estimation of $S_\perp$ also in Ref. [58]. In Fig. 5.15 the expression given in Eq. 5.2 was used in order to fit the data, with fit parameters also displayed in the figure, while in Fig. 5.16, a forth-order polynomial function was used to fit the data. In both Fig. 5.15 and Fig. 5.16, in the bottom plots, are displayed the qualities of the fits in terms of data/fit ratio, using the corresponding values for α = 1 in the case of pp collisions. The similar trends observed in pp and Pb-Pb collisions can be interpreted as the main features of the dynamical evolution of a collision are determined by the density of particles produced per unit of rapidity and unit of overlapping area, the size of the system playing a minor role.

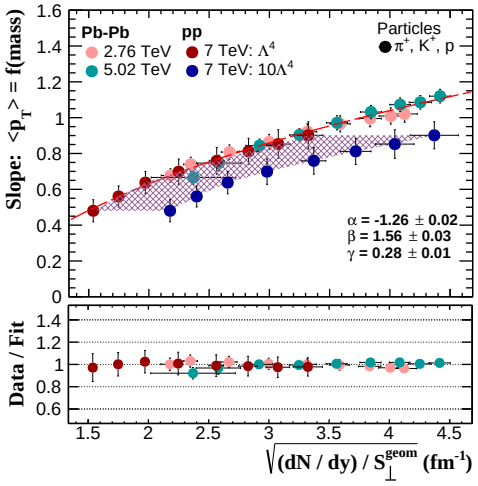

FIGURE 5.15: *Top:* The slope of the $< p_T >$ = f(mass) as a function of scaling variable, for Pb-Pb ($\sqrt{s_{NN}}$ = 2.76 and 5.02 TeV) and pp (α = 1: dark red markers; α = 10: dark blue markers), fitted with the expression given in Eq. 5.2; *Bottom:* The quality of the fit in terms of data/fit ratio [56].

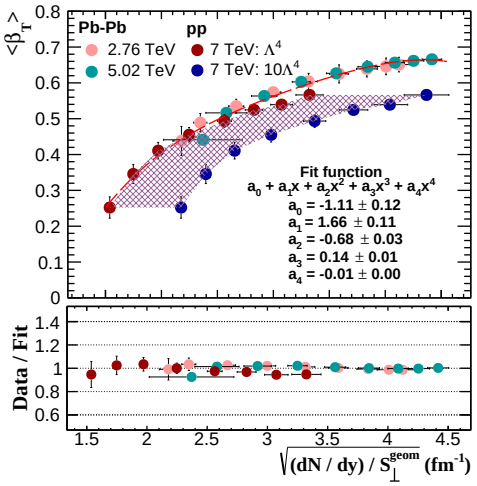

FIGURE 5.16: *Top:* The average values of the BGBW fit parameter, $< \beta_T >$, as a function of scaling variable, for Pb-Pb ($\sqrt{s_{NN}}$ = 2.76 and 5.02 TeV) and pp (α = 1: dark red markers; α = 10: dark blue markers), fitted with a 4^{th} order polynomial function; *Bottom:* The quality of the fit in terms of data/fit ratio [56].

6 | Summary and Outlook

In this thesis, based on the published data at RHIC and LHC, a systematic study was performed in terms of the dependence of different observables on the geometrical variable inspired from the CGC model, for a wide range of energies ($\sqrt{s_{NN}}$ from 7.7 GeV up to 5.44 TeV), for several colliding systems (Cu-Cu, Au-Au, Pb-Pb, Xe-Xe and pp) and centralities for A-A, or multiplicity classes for pp collisions.

The available experimental $< p_T >$ values follow a rather good scaling for these energies, with a jump from the highest available energy measured at RHIC to those at LHC. After fitting each $< p_T >$ = f($\sqrt{(dN/dy)/S_{\perp}^{geom}}$) with a straight line, the obtained slopes are showing a collision energy and mass dependent behavior: the slopes are increasing from pions to protons, while decreasing towards higher values of the collision energy (from BES to LHC). There was also evidenced a possible sign of gluon saturation for the most central collisions corresponding to LHC energies. The behavior of the experimental $< p_T >$ values as a function of the scaling variable supports the theoretical predictions from Ref. [42], where the $< p_T > / \sqrt{(dN/dy)/S_{\perp}}$ values were expected to decrease as a function of collision energy and centrality. A study of the core-corona effects for $\sqrt{s_{NN}}$ = 200 GeV, 2.76 TeV and 5.02 TeV was made. The results obtained for the core contribution in terms of $< p_T >$ and scaling variable and a comparison between these results and the experimental ones was also presented in this study. It was shown that if one takes into account only the core contribution, a better scaling was obtained, since the difference between the highest energy measured at RHIC and the LHC energies in terms of the $< p_T >$ slope as a function of $\sqrt{(dN/dy)/S_{\perp}}$ is reduced for the core contribution. Moreover, the $< p_T > / \sqrt{(dN/dy)/S_{\perp}}$ trend is also considerably attenuated. The saturation trend observed at the LHC energies for the most central collision is still observed for the core contribution.

In terms of the slope of the $< p_T >$ as a function of mass of pions, kaons and protons, its dependence on the scaling variable has shown a much better scaling, and also for the BGBW fit parameter, the average transverse flow velocity, $< \beta_T >$. The T_{kin}^{fo} and the offset of the $< p_T >$ = f($\sqrt{(dN/dy)/S_{\perp}}$) dependence are showing a jump between RHIC and LHC energies, possibly due to the interplay of other effects like suppression and its azimuthal dependence, or the hydrodynamic expansion in the final stages after hadronization that have to be carefully considered.

These similarities were also present in the pp and Pb-Pb comparison. A nice representation was obtained in terms of the $< p_T >$ dependence, where the pp and Pb-Pb systems have shown similar trends, while for the slope of the $< p_T >$ =

f(mass) and for the BGBW fit parameter, $< \beta_T >$, actual scalings were obtained, for the case of $\alpha = 1$.

This study supports the conclusion that the global features extracted from heavy ion collisions from the lowest RHIC energy, up to the highest LHC collision energy are dependent on the number of hadrons produced over unit of rapidity and unit of overlapping area, while the system size is playing a minor role.

In the near future we would like to extend this study to some unexploited, yet interesting observables. Based on the different behavior of heavier hadrons after the hadronization stage, the dependence on the geometrical variable of the different observables describing the hyperons should be carefully studied. Furthermore, new experimental data for pp collisions at a higher collision energy, i.e. 13 TeV, that will improve statistics in high multiplicity events, are now available. Moreover, in all these further studies, the core-corona contribution should be carefully taken into account.

Bibliography

[1] S. Schramm W. Greiner and E. Stein. *Quantum Chromodynamics*. 2007.

[2] S. Bethke. *J.Phys.G26:R27*, 2000.

[3] K. Fukushima and T. Hatsuda. *Rept.Prog.Phys.74:014001*, 2011.

[4] K. Rajagopal. *Nucl.Phys.A 661*, 1999.

[5] R. Plačakytė (on behalf of the H1 and ZEUS Collaborations). *Proceedings, 31st International Conference on Physics in collisions (PIC 2011): Vancouver, Canada, August 28-September 1, 2011*.

[6] H1 Collaboration. *Nucl.Phys.B 470 (1996), Eur.Phys.J.C 7:609 (1999)*.

[7] J. Jalilian-Marian F. Gelis, E. Iancu and R. Venugopalan. *Ann.Rev.Nucl.Part.Sci. 60*, 2010.

[8] T. Lappi and L. McLerran. *Nucl.Phys.A 772:200-212*, 2006.

[9] S.J. Sanders M.L. Miller, K. Reygers and P. Steinberg. *Ann.Rev.Nucl.Part.Sci.57:205-243*, 2007.

[10] K. Werner. *Phys.Rev.Lett. 98:152301*, 2007.

[11] K. Werner J. Aichelin. *Phys.Rev.C 79:064907*, 2009.

[12] K. Werner J. Aichelin. *Phys.Rev.C 82:034906*, 2010.

[13] M. Petrovici et al. *Phys.Rev.C 96:014908*, 2017.

[14] B.I. Abelev et al. (STAR Collaboration). *Phys.Rev.C 79:034909*, 2009.

[15] M. Sumbera (STAR Collaboration). *Acta Phys.Polon.Supp.6:429-436*, 2013.

[16] M. Petrovici et al. *AIP Conf.Proc. 1852:050003*, 2017.

[17] S. Horvat. *PhD Thesis: Measurement of the collision energy dependence of jet-quenching signatures of de-confinement at STAR*, 2017.

[18] S. Horvat (STAR Collaboration). *8th International Workshop on Critical Point and Onset of Deconfinement, March 11-15, Napa, California, USA*, 2013.

[19] J. Adams et al. (STAR Collaboration). *Phys.Rev.Lett. 91:172302*, 2003.

[20] ATLAS Collaboration. *JHEP 09:050*, 2015.

[21] ATLAS Collaboration. *ATLAS-CONF-2017-012*, 2017.

[22] B. Abelev et al. (ALICE Collaboration). *Phys.Rev.C 88:044910*, 2013.

[23] ALICE Collaboration. *Phys.Rev.Lett. 116:222302*, 2016.

[24] L. Kumar (STAR Collaboration). *Nucl.Phys.A, 904-905:256c-263c*, 2013.

[25] I. Adam et al. (ALICE Collaboration). *Phys.Rev.C 94:034903*, 2016.

[26] K. Aamodt et al. (ALICE Collaboration). *Phys.Rev.Lett. 105:252301*, 2010.

[27] B. Abelev et al. (ALICE Collaboration). *Phys.Rev.C 88:044910*, 2013.

[28] E. Schnedermann U. Heinz and J. Sollfrank. *Phys.Rev.C 48:2462*, 1993.

[29] ALICE Collaboration. *Phys.Lett.B 696:328*, 2011.

[30] B. Abelev et al. (ALICE Collaboration). *Phys.Lett.B 736:196-207*, 2014.

[31] H. Moreno. *Phys.Rev.D8*, 1973.

[32] A. Bialas and E. Bialas. *Acta.Phys.Polonica B5*, 1974.

[33] I. Dawson C. Buttar and A. Moraes. *Eur.Phys.J. C50*, 2007.

[34] ATLAS Collaboration. *ATL-PHYS-PUB-2010: 002*, 2010.

[35] A.H. Mueller. *Nucl.Phys.A 715:20c-34c*, 2003.

[36] V. Khachatryan et al. (CMS Collaboration). *J.High Energy Phys. 09:091*, 2010.

[37] D. Velicanu (CMS Collaboration). *J.Phys.G: Nucl.Part.Phys. 38:124051*, 2011.

[38] ALICE Collaboration. *Phys.Lett.B 708:249*, 2012.

[39] C. Andrei (ALICE Collaboration). *Nucl.Phys.A 931:c888*, 2014.

[40] V.A. Khoze Y.L. Dokshitzer and S. Troian. *J.Phys.G 17:1585*, 1991.

[41] T. Lappi. *Eur.Phys.J C71:1699*, 2011.

[42] E. Levin and A.J. Rezaeian. *Phys.Rev.D 83:114001*, 2011.

[43] B. Abelev et al. (ALICE Collaboration). *Phys.Rev.C 88:044910*, 2013.

[44] L. Adamczyk et al. (STAR Collaboration). *Phys.Rev.C 96:044904*, 2017.

[45] N. Jacazio (ALICE Collaboration). *Nucl.Phys.A 967:421*, 2017.

[46] X. Zhu (STAR Collaboration). *in Critical Point and Onset of Deconfinement (CPOD), 7-11.11.2011, Wuhan, China (unpublished)*, 2011.

[47] A.R. Timmins (STAR Collaboration). *Nucl.Phys.A 830:829c-832c*, 2009.

[48] J. Adams et al. (STAR Collaboration). *Phys.Rev.Lett. 98:062301*, 2007.

[49] M.M. Aggarwal et al. (STAR Collaboration). *Phys.Rev.C 83:024901*, 2011.

[50] B. Abelev et al. (ALICE Collaboration). *Phys.Rev.C 111:222301*, 2013.

[51] ALICE Collaboration. *Phys.Lett.B 728:216*, 2014.

[52] M. Šefčik et al. (ALICE Collaboration). *Eur.Phys.J. Web Conf. 171:13007*, 2018.

[53] J. Adam et al. (ALICE Collaboration). *Nat.Phys. 13:535*, 2017.

[54] U. Amaldi. *60 Years of CERN Experiments and Discoveries (World Scientific, Singapore)*, 2015.

[55] J. Adam et al. (ALICE Collaboration). *Phys.Rev.Lett. 116:222302*, 2016.

[56] M. Petrovici. A. Lindner et al. *Phys.Rev.C 98:024904*, 2018.

[57] P. Tribedy A. Bzdak, B. Schenke and R. Venugopalan. *Phys.Rev.C 87:064906*, 2013.

[58] M. Praszaowicz L. McLerran and B. Schenke. *Nucl.Phys.A 916:210*, 2013.

[59] J. Adam et al. (ALICE Collaboration). *Eur.Phys.J.C 75:226*, 2015.

[60] A.K. Dash (ALICE Collaboration). *DAE Symp.Nucl.Phys. 62:922*, 2017.

[61] R. Preghenella. *EPJ Web Conf. 171,* 17^{th} *International Conference on Strangeness in Quark Matter (SQM 2017):11003*, 2018.

[62] A. Schman H. Masui, A.M. Poskanzer and X. Sun. *Phys.Rev.C 91:024903*, 2015.

[63] L. Adamczyk et al. (STAR Collaboration). *Phys.Rev.C 93:014907*, 2016.

[64] F. Bellini (ALICE Collaboration). *Quark Matter*, 2018.

[65] D.S.D Albuquerque (ALICE Collaboration). *Quark Matter*, 2018.

[66] BRAHMS Collaboration. *Phys.Rev.C 94:014907*, 2016.

[67] STAR Collaboration. *Phys.Rev.Lett. 108:072301*, 2012.

[68] M. Petrovici. A. Lindner and A. Pop. *AIP Conf. Proc. 2076:040001*, 2019.

[69] A.A. Bylinkin and A.A. Rostovtsev. *Yad.Fiz. 75:1060 (Phys.At.Nuclei 75:999)*, 2012.